



## Covariance and climate signals among state-of-the-art tree-ring proxies

Philipp Römer<sup>a,\*</sup>, Anna Wieland<sup>b,\*\*</sup>, Max C.A. Torbenson<sup>a</sup>, Frederick Reinig<sup>a</sup>, Emanuele Ziaco<sup>a</sup>, Davide Frigo<sup>c</sup>, Markus Greule<sup>b</sup>, Otmar Urban<sup>d</sup>, Josef Čáslavský<sup>d</sup>, Natálie Pernicová<sup>d,e</sup>, Miroslav Trnka<sup>d,e</sup>, Marco Carrer<sup>c</sup>, Ulf Büntgen<sup>d,f,g</sup>, Frank Keppler<sup>b,h</sup>, Jan Esper<sup>a,d</sup>

<sup>a</sup> Department of Geography, Johannes Gutenberg University, 55099 Mainz, Germany

<sup>b</sup> Institute of Earth Sciences, Heidelberg University, 69120 Heidelberg, Germany

<sup>c</sup> Department of Land, Environment, Agriculture and Forestry, University of Padova, 35020 Legnaro, Italy

<sup>d</sup> Global Change Research Institute, Czech Academy of Sciences, 60300 Brno, Czech Republic

<sup>e</sup> Department of Agrosystems and Bioclimatology, Mendel University, 61300 Brno, Czech Republic

<sup>f</sup> Department of Geography, University of Cambridge, Cambridge CB2 3EN, UK

<sup>g</sup> Department of Geography, Faculty of Science, Masaryk University, 61137 Brno, Czech Republic

<sup>h</sup> Heidelberg Center for the Environment, Heidelberg University, 69120 Heidelberg, Germany

### ARTICLE INFO

Handling Editor: Dr P Rioual

#### Keywords:

Mediterranean  
Paleoclimatology  
*Pinus heldreichii*  
Quantitative wood anatomy  
Tree-ring stable isotopes

### ABSTRACT

Tree-ring stable isotopes and wood anatomical traits emerged as powerful proxies for paleoclimate reconstructions, providing information beyond traditional ring width and wood density chronologies. However, comprehensive comparisons of these state-of-the-art tree-ring proxies derived from the same trees have yet to be performed to identify and differentiate their full paleoclimatic skill. Here, we assess covariance and climate signals in tree-ring width (TRW), maximum latewood density (MXD), cellulose stable carbon ( $\delta^{13}\text{C}_c$ ) and oxygen ( $\delta^{18}\text{O}_c$ ) isotopes, lignin methoxy carbon ( $\delta^{13}\text{C}_m$ ) and hydrogen ( $\delta^2\text{H}_m$ ) isotopes, radial cell lumen diameter ( $D_{\text{rad}}$ ), and radial and tangential cell wall thickness ( $\text{CWT}_{\text{rad}}/\text{CWT}_{\text{tan}}$ ) of ten Bosnian pines (*Pinus heldreichii*) from a treeline site on Mt. Smolikas, Greece. Proxy cross-comparison over the period 1861–2020 CE reveals strong covariance between detrended  $\delta^{13}\text{C}_c$  and  $\delta^{13}\text{C}_m$  ( $r \geq 0.81$ ).  $\delta^{13}\text{C}_c$  and  $\delta^{18}\text{O}_c$  exhibit the highest inter-series correlations ( $r \geq 0.61$ ) among all proxies.  $\delta^{13}\text{C}_c$ ,  $\delta^{13}\text{C}_m$ ,  $\delta^{18}\text{O}_c$ , together with  $D_{\text{rad}}$ , show considerable skill for reconstructing summer precipitation, whereas MXD and  $\delta^2\text{H}_m$  may be used for summer temperature reconstructions. Enhanced inter-series and hydroclimate correlations, along with a prolonged seasonality are significant advances of the isotopic and wood anatomical measurements compared to TRW. Our findings highlight the importance of integrating new isotopic, particularly  $\delta^{13}\text{C}_c$ , and xylem anatomical data into existing TRW networks to enhance our understanding of past hydroclimate variability and contextualize the recent aridification of the Mediterranean region.

### 1. Introduction

The Mediterranean region is facing significant environmental and socio-economic challenges due to the increasing intensity, frequency, and duration of heatwaves and droughts since the late 20th century and the start of the 21st century (Cramer et al., 2018). The limited number of annually resolved climate reconstructions dating back to the 1st millennium CE, however, constrains our ability to place recent hydrothermal dynamics into a long-term context of natural climate variability.

New millennium-length climate reconstructions are therefore urgently needed to disentangle the roles of natural and anthropogenic forcings in the recent aridification of the Mediterranean (Hoerling et al., 2012; Lionello and Scarascia, 2018; Spinoni et al., 2019).

The *Pinus heldreichii* treeline ecotone on Mt. Smolikas (Fig. 1a) in northern Greece is so far the only Mediterranean location where tree-ring width (TRW) and maximum latewood density (MXD) measurements enabled high-resolution climate estimates beyond the Medieval Warm Period (Esper et al., 2020a, 2021; Klippel et al., 2018, 2019). The

\* Corresponding author.

\*\* Corresponding author.

E-mail addresses: [phiroeme@uni-mainz.de](mailto:phiroeme@uni-mainz.de) (P. Römer), [anna.wieland@geow.uni-heidelberg.de](mailto:anna.wieland@geow.uni-heidelberg.de) (A. Wieland).

Mt. Smolikas record, which extends back to the 5th century CE, represents the best-replicated tree-ring chronology from a high-elevation southern European site during the 1st millennium CE (Luterbacher et al., 2012; Römer et al., 2021). However, the TRW-based hydroclimate reconstructions lack distinct low-frequency information due to the detrending required to remove ontogenetic trends in growth and mitigate the heteroscedastic nature of these data (Bräker, 1981; Osborn et al., 1997). The existing reconstructions may thus not capture the entire spectrum of hydroclimate variability, underscoring the need for alternative proxies to complete our understanding of high-to-low frequency climate fluctuations in the Eastern Mediterranean (Büntgen, 2022).

Tree-ring stable isotopes (TRSI) derived from wood cellulose, including stable carbon ( $\delta^{13}\text{C}_c$ ), oxygen ( $\delta^{18}\text{O}_c$ ), and hydrogen ( $\delta^2\text{H}_c$ ) isotopes, have proven valuable for reconstructing past climate variability at interannual to multimillennial timescales (Büntgen et al., 2021; Nakatsuka et al., 2020; Yang et al., 2021). TRSI measurements often lack ontogenetic trends and thus do not require standardization (Büntgen et al., 2020; Gagen et al., 2007; Young et al., 2011), exhibit strong inter-series correlations (Hartl-Meier et al., 2015; Treydte et al., 2007), and require small sample sizes to create reliable site chronologies (Belmecheri et al., 2022; Römer et al., 2023). In the Mediterranean,  $\delta^{13}\text{C}_c$  and  $\delta^{18}\text{O}_c$  revealed great potential for reconstructing past summer precipitation (Dorado Liñán et al., 2012; Levanić et al., 2020; Lukać et al., 2021), temperature (Esper et al., 2015a; Szymczak et al., 2012), and drought variability (An et al., 2023; Freund et al., 2023).

In recent decades, isotopic measurements of carbon and hydrogen on lignin methoxy groups (Fig. 1b) have emerged as valuable climate proxies, providing a fast and cheap alternative to cellulose isotopic measurements (Greule et al., 2008, 2009; Keppler et al., 2007).  $\delta^2\text{H}$  values of lignin methoxy groups ( $\delta^2\text{H}_m$ ) are unaffected by the evaporative  $^2\text{H}$  enrichment of leaf water and thus closely reflect the  $\delta^2\text{H}$  values of precipitation, which are predominantly controlled by air temperature (Dansgaard, 1964), making  $\delta^2\text{H}_m$  a promising temperature proxy in mid-to-high latitudes (Anhäuser et al., 2017, 2020; Feakins et al., 2013;

Greule et al., 2021; Keppler et al., 2007; Lu et al., 2020). Lignin methoxy  $\delta^{13}\text{C}$  ( $\delta^{13}\text{C}_m$ ) has shown a similar temperature sensitivity at selected sites in Europe (Gori et al., 2013; Riechelmann et al., 2016; Wieland et al., 2022) and Asia (Lu et al., 2020; Wang et al., 2020).

In addition, methodological advances in quantitative wood anatomy (QWA) have opened new research perspectives for paleoclimatology (Prendin et al., 2017; von Arx and Carrer, 2014). The quantification of anatomical features improved the spatiotemporal resolution of traditional proxies and allowed to disentangle the effects of environmental conditions on the structural properties of the xylem at the cellular level (Fonti et al., 2010; Pandey, 2021). Among numerous xylem anatomical traits, tracheid lumen area, radial lumen diameter ( $D_{\text{rad}}$ ), cell wall thickness (CWT), and inferred wood anatomical densities have proven to be reliable climate predictors (Balanzategui et al., 2021; Björklund et al., 2020, 2023; Carrer et al., 2018; González-Cázares et al., 2019; Lopez-Saez et al., 2023; Ziaco et al., 2016).

Using samples from ten living Bosnian pines from Mt. Smolikas (Greece), we here combine TRW, MXD,  $\delta^{13}\text{C}_c$ ,  $\delta^{18}\text{O}_c$ ,  $\delta^{13}\text{C}_m$ ,  $\delta^2\text{H}_m$ ,  $D_{\text{rad}}$ , and CTW measurements to assess covariance both within and among these state-of-the-art tree-ring proxies and their climate sensitivities. We evaluate whether specific proxies may be combined and provide recommendations on the suitability of individual proxies for future paleoclimate research in the Mediterranean.

## 2. Material and methods

### 2.1. TRW and MXD measurements

Between 2015 and 2019, a total of 878 core and disc samples were collected from living and relict Bosnian pines (*Pinus heldreichii* H. Christ) on Mt. Smolikas in Greece (40.1°N/21.0° E,  $\geq 2000$  m a.s.l.) to establish well-replicated TRW ( $n = 878$  series) and MXD ( $n = 192$  series) chronologies (Esper et al., 2020a, 2021). In 2021, ten of the living pines were resampled to develop new stable isotopic and wood anatomical records extending to 2020 CE. Two 1-cm increment cores were extracted from

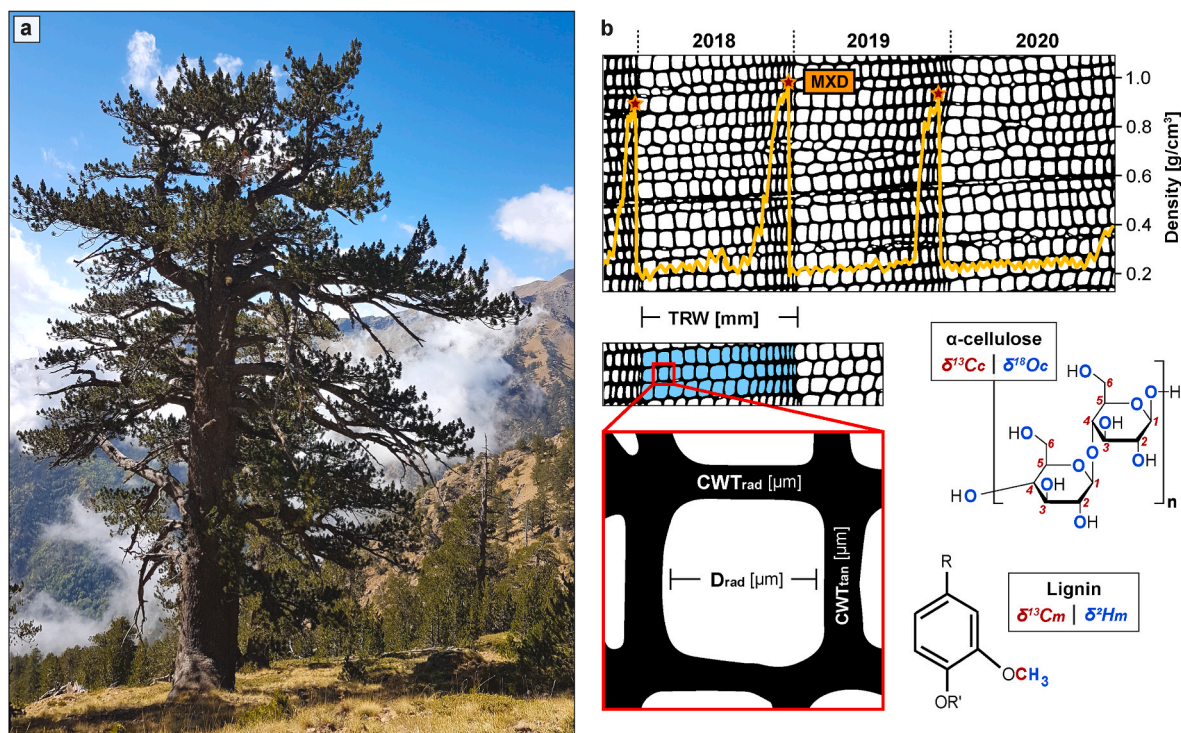


**Fig. 1.** Study material and tree-ring data. (a) Living Bosnian pine on Mt. Smolikas. (b) Illustration of tree-ring width (TRW), maximum latewood density (MXD), radial cell lumen diameter ( $D_{\text{rad}}$ ), radial and tangential cell wall thickness ( $\text{CWT}_{\text{rad}}/\text{CWT}_{\text{tan}}$ ), cellulose carbon ( $\delta^{13}\text{C}_c$ ) and oxygen isotopes ( $\delta^{18}\text{O}_c$ ), as well as methoxy carbon ( $\delta^{13}\text{C}_m$ ) and hydrogen ( $\delta^2\text{H}_m$ ) isotopes.

each tree at breast height (~1.3 m) from the same stem direction (~5 cm above each other) perpendicular to the slope. TRW was measured on each core with an accuracy of 0.01 mm using the high-precision LINTAB 6 device (Rinntech, Heidelberg, Germany) and TSAP-Win software (Rinn, 2012). Dating precision was verified by comparing the new TRW data with the old measurements (Figs. S1a–b). One core each was used for isotopic and anatomical analyses. No MXD measurements were performed on the new samples. However, to ensure a robust comparison between MXD and the other proxies, a subset of ten living-tree series was selected from the data used in Esper et al. (2020a) to create a representative MXD record (Figs. S1c–d) with a sample replication equal to the other proxies. A detailed description of the MXD methodology is provided in Klippel et al. (2019).

## 2.2. Stable isotope measurements

The isotopic measurements of  $\delta^{13}\text{C}_c$ ,  $\delta^{13}\text{C}_m$ ,  $\delta^{18}\text{O}_c$ , and  $\delta^2\text{H}_m$  were performed at annual resolution on the same increment cores. The tree rings of each sample were carefully separated with a scalpel, cut into smaller pieces, and divided equally into two Eppendorf microtubes for cellulose and methoxy isotope measurements. When cutting and partitioning, care was taken to ensure that the microtubes contained the original earlywood-latewood proportions.

For cellulose isotopic measurements,  $\alpha$ -cellulose was extracted via the modified Jayme-Wise isolation method (Boettger et al., 2007) at the Global Change Research Institute, Czech Republic (details in Wieland et al., 2024). After extraction, 0.5–1.0 mg of  $\alpha$ -cellulose was placed in tin ( $\delta^{13}\text{C}_c$ ) and silver ( $\delta^{18}\text{O}_c$ ) capsules. The tin capsules were combusted to  $\text{CO}_2$  at 960 °C, while the silver capsules were pyrolyzed to CO at 1450 °C using the high-temperature cell of the varioPYRO cube elemental analyzer (Elementar Analysensysteme, Langenselbold, Germany). The ratios of heavy to light carbon ( $^{13}\text{C}/^{12}\text{C}$  from  $\text{CO}_2$ ) and oxygen ( $^{18}\text{O}/^{16}\text{O}$  from CO) isotopes were measured using the ISOPRIME100 continuous-flow isotope ratio mass spectrometer (IRMS) (Isoprime, Manchester, UK). Isotopic measurements were calibrated using certified reference materials from the International Atomic Energy Agency (IAEA) and the United States Geological Survey (USGS).  $^{13}\text{C}/^{12}\text{C}$  ratios were referenced to caffeine (IAEA-600) and graphite (USGS24), and  $^{18}\text{O}/^{16}\text{O}$  ratios to benzoic acid (IAEA-601 and IAEA-602).

Isotopic measurements on lignin methoxy groups were performed at the Institute of Earth Sciences, Heidelberg University (Germany), using the modified Zeisel method (Greule et al., 2008, 2009; Keppler et al., 2004, 2007) in which gaseous iodomethane ( $\text{CH}_3\text{I}$ ) is formed from the reaction between methyl ethers and esters and hydroiodic acid (Zeisel, 1885). For this, 5 mg ( $\delta^{13}\text{C}_m$ ) and 7 mg ( $\delta^2\text{H}_m$ ) of wooden material and 250  $\mu\text{l}$  of hydroiodic acid were heated in crimp glass vials for 30 min at 130 °C, followed by a sample equilibration at room temperature. Ten to 90  $\mu\text{l}$  aliquot of headspace were injected via an autosampler (A200S, CTC Analytics, Zwingen, Switzerland) into a gas chromatograph (HP 6890N, Agilent, Santa Clara, USA) equipped with a combustion reactor [ceramic tube ( $\text{Al}_2\text{O}_3$ ), length 320 mm, 0.5 mm i.d., Cu/Ni/Pt wires inside (activated by oxygen)] for  $\delta^{13}\text{C}_m$  measurements or a thermo conversion reactor [ceramic tube ( $\text{Al}_2\text{O}_3$ ), length 320 mm, 0.5 mm i.d.] for  $\delta^2\text{H}_m$  measurements.  $\text{CH}_3\text{I}$  was oxidized to  $\text{CO}_2$  at 960 °C and pyrolyzed to  $\text{H}_2$  at 1450 °C. The two resulting gases were transferred through a Finnigan GC-Combustion III interface into a Thermo Finnigan DeltaplusXL IRMS (Thermo Fisher Scientific, Waltham, USA) to measure the ratio of heavy to light carbon ( $^{13}\text{C}/^{12}\text{C}$  from  $\text{CO}_2$ ) and hydrogen ( $^2\text{H}/^1\text{H}$  from  $\text{H}_2$ ) isotopes. The isotope measurements were normalized using HUBG reference materials (Greule et al., 2019, 2020). HUBG2 and HUBG4 were used for the  $\delta^{13}\text{C}_m$  measurements, and HUBG1 and HUBG3 for  $\delta^2\text{H}_m$  measurements.

Isotope ratios are expressed in the conventional  $\delta$  notation in Urey (Ur) relative to the Vienna Pee Dee Belemnite standard ( $\delta^{13}\text{C}$ ) and the Vienna Standard Mean Ocean Water ( $\delta^{18}\text{O}_c$  and  $\delta^2\text{H}_m$ ). One mUr is equivalent to 1 per mille (Brand and Coplen, 2012). The ion sources of

the IRMS systems were centered, tuned, and tested for stability ( $\sigma < 0.03$  mUr for  $\delta^{13}\text{C}_c$ ,  $< 0.02$  mUr for  $\delta^{13}\text{C}_m$ ,  $< 0.02$  mUr for  $\delta^{18}\text{O}_c$ ,  $< 0.04$  mUr for  $\delta^2\text{H}_m$ , on ten pulses of monitoring gas) and linearity ( $< 0.04$  mUr/nA for  $\delta^{13}\text{C}_c$ ,  $< 0.06$  mUr/V for  $\delta^{13}\text{C}_m$ ,  $< 0.04$  mUr/nA for  $\delta^{18}\text{O}_c$ ,  $< 1$  mUr/V for  $\delta^2\text{H}_m$ ) before each sequence of isotopic measurements. The  $\text{H}_3^+$  factor was quantified before each set of  $\delta^2\text{H}_m$  measurements ( $< 3.5$  ppm/nA). Six (cellulose) and five (methoxy group) consecutive measurements on the same samples were performed to assess the precision of the isotopic measurements. Average standard deviations were 0.04 mUr for  $\delta^{13}\text{C}_c$ , 0.09 mUr for  $\delta^{18}\text{O}_c$ , between 0.01 and 0.25 mUr for  $\delta^{13}\text{C}_m$ , and between 0.5 and 2 mUr for  $\delta^2\text{H}_m$ .

## 2.3. Quantitative wood anatomy

To produce high-quality wood anatomical images, increment cores were cut into 4–5 cm long pieces and boiled in distilled water. Ten micrometer [ $\mu\text{m}$ ] thick transverse microsections were cut from each piece using a rotary microtome (Leica, Wetzlar, Germany). The microsections were bleached in 10% NaOCl for 10 min, stained with a 1:1 safranin and astra blue solution, dehydrated successively in 50% and 100% ethanol baths, and permanently mounted on microscope slides with Euparal (Carl Roth, Karlsruhe, Germany). The permanent slides were scanned at a resolution of 2.2 pixels/ $\mu\text{m}$  using a Hamamatsu NanoZoomer slide scanner (Hamamatsu Photonics, Shizuoka, Japan).

The obtained digital images were processed using ROXAS v4.0 (von Arx and Carrer, 2014; Prendin et al., 2017) to quantify xylem anatomical traits, including radial cell lumen diameter ( $D_{\text{rad}}$ ) as well as radial and tangential cell wall thickness ( $\text{CWT}_{\text{rad}}/\text{CWT}_{\text{tan}}$ ). After the automated detection of individual cells by ROXAS, a manual editing was performed to remove incorrectly recognized features such as resin ducts and parenchyma cells. Tree-ring sequences were crossdated by comparing the TRW output of ROXAS with the LINTAB measurements. To quantify intra-annual variability in the wood anatomical structures, we computed standardized tracheidograms (Vaganov, 1990; Ziaco, 2020) by aligning cell radial files for each ring using the R package RAPTOR (Peters et al., 2018), normalizing cell numbers to 30 using the *tgram* function, and dividing each ring into ten tangential sectors. Tree-ring sectoring allows for the refinement of climatic signals encoded in xylem cellular traits (Ziaco and Liang, 2019), with ten sectors generally considered an appropriate compromise between higher temporal resolution and maintaining a reliable cell count in each sector (Belokopytova et al., 2019; Carrer et al., 2018). A principal component analysis (PCA) was applied to assess similarities and differences between the sectorial QWA chronologies and the annual TRW, MXD, and TRSI chronologies. Principal components (PCs) were tested for significance using randomization tests and the Rnd-Lambda stopping rule (Peres-Neto et al., 2005).

## 2.4. Data treatment and chronology development

To account for the depletion of atmospheric  $^{13}\text{C}$  due to anthropogenic  $\text{CO}_2$  emissions,  $\delta^{13}\text{C}_c$  and  $\delta^{13}\text{C}_m$  series were corrected for the Suess effect (Keeling, 1979) by adding residuals to pre-industrial levels of  $-6.41$  mUr to the tree-ring values after 1860 CE (Fig. S2). The atmospheric  $^{13}\text{C}$  data were obtained from McCarroll and Loader (2004) and the Mauna Loa Observatory (<https://scrippsco2.ucsd.edu>; Keeling et al., 2005). Both  $\delta^{13}\text{C}$  records were further corrected for the increasing leaf-internal  $^{13}\text{C}$  discrimination under elevated  $\text{CO}_2$  concentrations using a LOESS regression model proposed by McCarroll et al. (2009). However, since the latter so-called pin-correction was developed using cellulose-derived isotope data and its application might lead to increasing uncertainty in the isotopic measurements on methoxy groups, we used the Suess-effect-corrected  $\delta^{13}\text{C}$  data for inter-proxy comparisons and climate calibration. Results on the pin-corrected  $\delta^{13}\text{C}$  data can be found in the supplementary material.

The individual time series of each proxy were detrended using the ARSTAN software (Cook et al., 2017) by calculating residuals from

horizontal means (HOM) and cubic smoothing splines with 50% frequency cutoffs at 100 years (100SP) and 30 years (30SP) to emphasize high-to-low frequency variance. Tree-ring data were power-transformed and variance-stabilized (Cook and Peters, 1997; Frank et al., 2007) and mean chronologies were developed by computing the bi-weight robust means of the individual series. Series covariance was assessed by calculating average inter-series correlations ( $R_{\text{bar}}$ ) over the 1861–2020 CE common period (Wigley et al., 1984), except for MXD which was confined to 1861–2017 CE.

## 2.5. Meteorological data and climate signal detection

The proxy chronologies were correlated against monthly temperature, precipitation and cloud cover data (CRU TS4.07, Harris et al., 2020), as well as against the Palmer Drought Severity Index (PDSI, Wells et al., 2004). The meteorological data were retrieved for the closest  $0.5^\circ$  grid (40.0–40.5°N/20.5–21.0°E) using the KNMI climate explorer (<http://climexp.knmi.nl>). To reduce uncertainty arising from the limited number of meteorological stations reaching back to the early 20th century (Fig. 2), climate correlations were calculated for 1931–2020 CE. The year 1931 CE was selected as the starting year as two nearby precipitation stations (Kerkyra and Thessaloniki) are included in the grid thereafter. The meteorological data were tested for normal distribution and climate-proxy relationships assessed by using Pearson (temperature and cloud cover) and Spearman rank (precipitation and PDSI) correlations. Prior to the correlation calculations, the climate data were standardized the same way as the tree-ring data. Thirty-one-year running and field correlations were computed to test the temporal robustness and spatial extent of the climate signals.

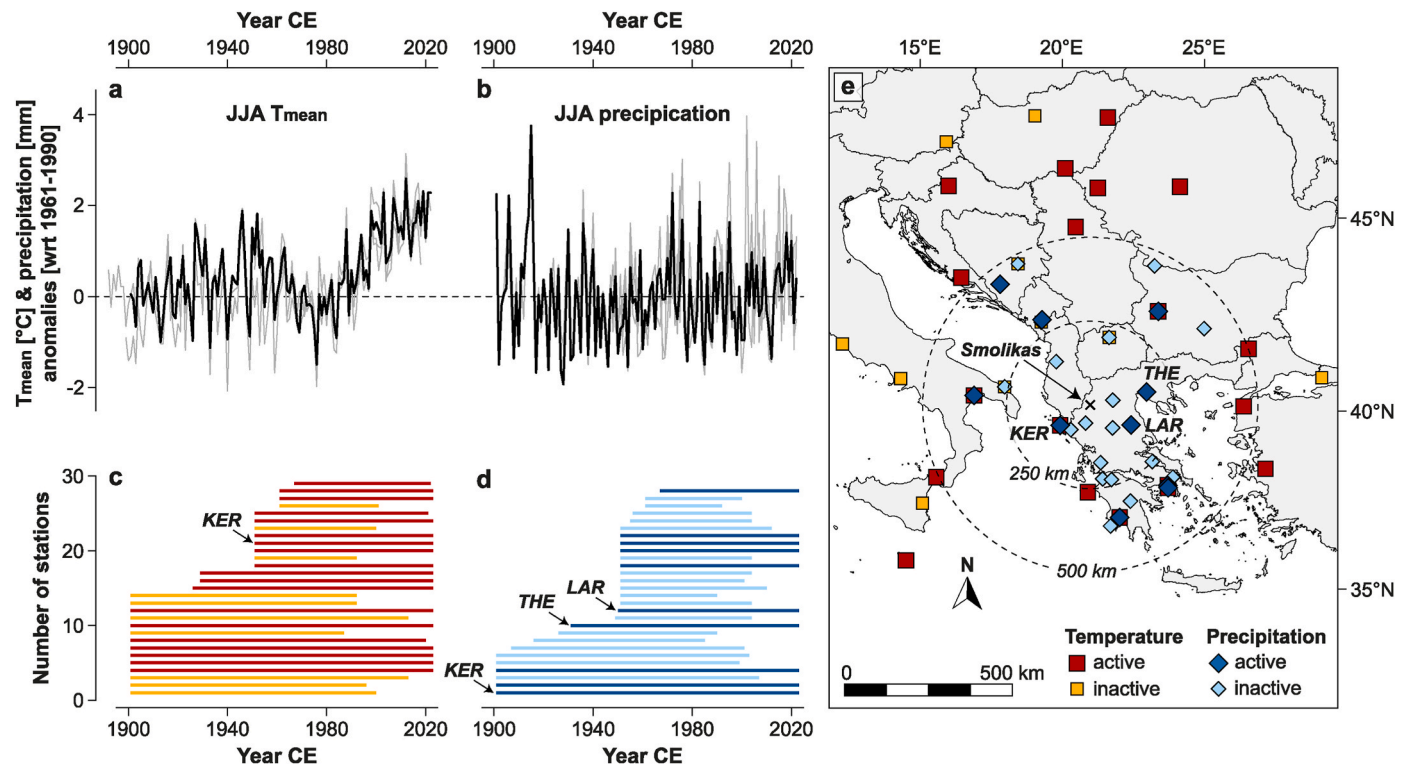


**Fig. 2.** Climate data. June–August (JJA) (a) mean air temperature ( $T_{\text{mean}}$ ) and (b) precipitation anomalies (wrt. 1961–1990 CE) from the CRU TS4.07 grid (black lines) nearest to Mt. Smolikas and the meteorological stations (grey lines) in Kerkyra (KER), Larissa (LAR), and Thessaloniki (THE). (c–d) Temporal coverage of the temperature and precipitation stations used to interpolate the gridded data. Each horizontal bar represents one station. The dark red and dark blue bars highlight (“active”) stations providing measurements until 2020 CE. (e) Spatial coverage of the “active” and “inactive” stations integrated into the gridded data. The dashed circles indicate linear distances (250 and 500 km) from the study site. (For interpretation of the references to color in this figure legend, the reader is referred to the Web version of this article.)

## 3. Results

### 3.1. Proxy characteristics and covariance

Mean cambial age of the TRW, TRSI, and QWA series ranges from 298 years in 1861 to 457 years in 2020 CE. In contrast, the MXD series are, on average,  $\sim 40$  years younger (Fig. S3) and terminate in 2017 CE. Mean segment lengths (MSL) vary slightly among the proxies due to different measurement periods, ranging from 157 years in  $\delta^{13}\text{C}_m$  and  $\delta^2\text{H}_m$  to 218 years in  $D_{\text{rad}}$  and CWT. However, all proxy chronologies are well replicated ( $n \geq 8$  series) over the 1861–2020 CE period (Table 1).

The raw TRW and CWT ( $\text{CWT}_{\text{rad}}$  and  $\text{CWT}_{\text{tan}}$ ) chronologies show the highest first-order autocorrelations ( $\text{AC1} \geq 0.65$ ) for 1861–2020 CE.  $\text{AC1}$  is higher in methoxy ( $\text{AC1}_{\text{raw}} = 0.41$ ) than in cellulose isotopes ( $\text{AC1}_{\text{raw}} \leq 0.30$ ), reflecting the stronger trends in  $\delta^{13}\text{C}_m$  ( $+0.004 \text{ mUr yr}^{-1}$ ) and  $\delta^2\text{H}_m$  ( $-0.03 \text{ mUr yr}^{-1}$ ) from 1861 to 2020 CE (Fig. 3).  $\delta^{13}\text{C}_c$  values decrease on average by  $-0.002 \text{ mUr yr}^{-1}$  and  $\delta^{18}\text{O}_c$  values increase by  $+0.001 \text{ mUr yr}^{-1}$  in the same period. TRW and  $D_{\text{rad}}$  values increase by  $+0.002 \text{ mm yr}^{-1}$  and  $+0.008 \mu\text{m yr}^{-1}$ , while trends in CWT and MXD are  $<0.001 \mu\text{m yr}^{-1}$  and  $\text{g cm}^{-3} \text{ yr}^{-1}$ . Similar  $\text{AC1}$  values between the raw and HOM-detrended data indicate retention of low-frequency variability after detrending. Lower  $\text{AC1}$  values after spline detrending demonstrate the removal of this low-frequency information, but coincide with an increase in covariance among series. The spline-detrended  $\delta^{13}\text{C}_c$  and  $\delta^{18}\text{O}_c$  series exhibit the highest  $R_{\text{bar}} \geq 0.61$ .  $R_{\text{bar}}$  values of the methoxy isotopes are noticeably lower and similar to those of TRW and  $D_{\text{rad}}$ . MXD,  $\text{CWT}_{\text{rad}}$ , and  $\text{CWT}_{\text{tan}}$  indicate the lowest  $R_{\text{bar}} \leq 0.28$  (Fig. S4).

The Suess-effect-corrected  $\delta^{13}\text{C}_c$  values fluctuate around  $-21.83 \pm 0.83 \text{ mUr}$  and are on average  $3.15 \text{ mUr}$  higher than the  $\delta^{13}\text{C}_m$  values ( $-24.98 \pm 1.14 \text{ mUr}$ ). However, high correlations ( $r = 0.81$ ,  $p < 0.001$ )

**Table 1**

Proxy characteristics.

Proxy	n	Period ( $\geq 5$ series)	MSL $\pm 1\sigma$	AC1 RAW   HOM   100SP   30SP	Rbar HOM   100SP   30SP
TRW	10	1810–2020	205 $\pm$ 47	0.72   0.73   0.56   0.25	0.38   0.34   0.37
MXD	10	1810–2017	201 $\pm$ 47	0.53   0.53   0.36   0.16	0.18   0.23   0.28
$\delta^{13}C_c$	10	1810–2020	205 $\pm$ 47	0.30   0.30   0.16   0.00	0.56   0.62   0.67
$\delta^{13}C_m$	10	1861–2020	157 $\pm$ 07	0.41   0.43   0.18   -0.01	0.40   0.30   0.33
$\delta^{18}O_c$	10	1810–2020	205 $\pm$ 47	0.25   0.25   0.16   0.06	0.39   0.61   0.62
$\delta^2H_m$	10	1861–2020	157 $\pm$ 07	0.41   0.41   0.24   0.09	0.34   0.36   0.40
$D_{rad}$	10	1807–2020	218 $\pm$ 47	0.45   0.45   0.16   0.00	0.27   0.36   0.43
$CWT_{rad}$	10	1807–2020	218 $\pm$ 47	0.65   0.65   0.48   0.18	0.08   0.15   0.21
$CWT_{tan}$	10	1807–2020	218 $\pm$ 47	0.65   0.65   0.46   0.21	0.12   0.17   0.22

n: total number of series. **MSL**: mean segment length  $\pm 1$  standard deviation ( $1\sigma$ ). **AC1**: first-order autocorrelation of the raw and detrended chronologies. **Rbar**: average inter-series correlation between the detrended series. The latter two statistics are calculated for 1861–2020 CE (MXD for 1861–2017 CE).

between the spline-detrended  $\delta^{13}C$  chronologies indicate a close association between  $\delta^{13}C_c$  and  $\delta^{13}C_m$ . Inter-proxy correlations are overall higher after the 30SP detrending than after the 100SP detrending (Table 2). The 30SP-detrended  $\delta^{13}C$  records are positively correlated with MXD ( $r \geq 0.51$ ) and  $\delta^{18}O_c$  ( $r \geq 0.44$ ), and negatively correlated with  $D_{rad}$  ( $r \leq -0.32$ ), with overall higher correlations for  $\delta^{13}C_c$  than for  $\delta^{13}C_m$ .  $\delta^{18}O_c$  is most strongly correlated with  $\delta^{13}C_c$  ( $r = 0.59$ ) and  $D_{rad}$  ( $r = -0.51$ ).  $\delta^2H_m$  displays negative correlations with MXD and  $CWT_{rad}$  ( $r \leq -0.28$ ) and a positive correlation with  $D_{rad}$  ( $r = 0.30$ ). TRW is positively correlated with  $D_{rad}$  and  $CWT_{tan}$  ( $r = 0.41$ ), while MXD shows significant ( $p < 0.001$ ) correlations with all proxies except TRW. A correlation of  $r = 0.71$  between  $CWT_{tan}$  and  $CWT_{rad}$  indicates a strong association between the two CWT orientations, but only  $CWT_{rad}$  shows significant ( $p < 0.001$ ) correlations with  $\delta^{18}O_c$ ,  $\delta^2H_m$ , and  $D_{rad}$ .

### 3.2. Climate signals

Climate signals are most distinct in summer and after the 30SP detrending, but the maximum seasonal responses vary slightly among the proxies (Fig. 4). TRW correlations with mean air temperature ( $T_{mean}$ ), precipitation, and the PDSI are all non-significant ( $p > 0.01$ ) for 1931–2020 CE. Significant ( $p < 0.01$ ) TRW correlations are restricted to June–July (JJ) cloud cover ( $r = 0.28$ ) and diurnal temperature range ( $r = -0.38$ ; Fig. S5). MXD shows the highest correlations with July–September  $T_{mean}$  ( $r = 0.55$ ), precipitation ( $r = -0.41$ ) and cloud cover data ( $r = -0.62$ ). TRW and MXD correlations with the PDSI are non-significant for all months, except for MXD in September. TRW and MXD correlations with previous-year climate are weak and only significant between 30SP-detrended MXD and July  $T_{mean}$  ( $r = -0.29$ ), as well as between TRW and August precipitation ( $r = 0.32$ ) and cloud cover ( $r = 0.33$ ; Fig. S6).

The 30SP-detrended  $\delta^{13}C_c$ ,  $\delta^{13}C_m$ , and  $\delta^{18}O_c$  data show the highest correlations with June–August (JJA)  $T_{mean}$  ( $r = 0.52/0.40/0.40$ ), precipitation ( $r = -0.69/-0.55/-0.55$ ), and cloud cover data ( $r = -0.64/-0.50/-0.55$ ,  $p < 0.001$ ). Correlations with the PDSI are overall lower and range from  $r = -0.38$  in  $\delta^{18}O_c$  to  $r = -0.49$  in  $\delta^{13}C_c$ . While the correlations with JJA precipitation are temporally stable for all detrendings,  $T_{mean}$  correlations decrease towards the lower frequency domain (Fig. 5). Spectral coherence analyses between the isotope and climate data support these findings and point to precipitation as the dominant

climatic factor for  $\delta^{13}C_c$ ,  $\delta^{13}C_m$ , and  $\delta^{18}O_c$  variability (Fig. S7). Similar results are found for the pin-corrected  $\delta^{13}C$  data (Fig. S8). For  $\delta^2H_m$ , the highest correlation is found with June–September (JJAS)  $T_{mean}$  ( $r = -0.44$ ,  $p < 0.001$ ), while no significant correlations are obtained with precipitation. Running correlations between  $\delta^2H_m$  and JJAS  $T_{mean}$  are stable over time and for all detrendings, but  $\delta^2H_m$  lacks significant coherence with temperature data at mid-to-low frequencies ( $\sim 2$ – $4$  and  $> 10$  years; Fig. S9). Correlations between TRSIs and previous-year climate data are weak and significant ( $p < 0.01$ ) only for  $\delta^{13}C$  and August  $T_{mean}$  ( $r = -0.29$  for  $\delta^{13}C_c$  and  $-0.33$  for  $\delta^{13}C_m$ ), and for  $\delta^2H_m$  and June  $T_{mean}$  ( $r = -0.31$ ).

The climate sensitivity of  $D_{rad}$  is inverse to that of  $\delta^{13}C_c$ ,  $\delta^{13}C_m$ , and  $\delta^{18}O_c$ , yet similar in terms of seasonality and strength. The annual  $D_{rad}$  chronology, which represents the average radial lumen diameter of earlywood and latewood cells, shows the highest 30SP correlations with JJA precipitation ( $r = 0.56$ ),  $T_{mean}$  ( $r = -0.55$ ), and cloud cover data ( $r = 0.62$ , all  $p < 0.001$ ). Although 30SP correlations between  $D_{rad}$  and cloud cover are slightly higher than those with precipitation, considerably lower correlations obtained for the HOM-detrended data ( $r = 0.43$ ) indicate a stronger low-frequency coherence with precipitation ( $r = 0.60$ ; Fig. S10). The 30SP correlations with the PDSI are significant from August to October ( $r = 0.28$ – $0.34$ ,  $p < 0.01$ ) and about as strong as with previous-year June  $T_{mean}$  ( $r = 0.38$ ).  $CWT_{rad}$  and  $CWT_{tan}$  indicate almost no significant climate correlations at annual resolution. Only  $CWT_{rad}$  significantly correlates with September  $T_{mean}$  ( $r = 0.28$ ) and cloud cover in current and previous August ( $r = -0.28$  and  $0.28$ ,  $p < 0.01$ ).

### 3.3. QWA sector chronologies

The total QWA data comprise  $\sim 2.5$  million individual cell measurements. The ten anatomical sectors, ranging from the early- (I) to the latewood (X), represent the intra-annual variability of  $D_{rad}$ ,  $CWT_{rad}$ , and  $CWT_{tan}$  from 1861 to 2020 CE (Fig. 6a).  $D_{rad}$  decreases from  $30.3 \pm 4.2 \mu m$  ( $\pm 1\sigma$ , sector I) to  $6.7 \pm 1.5 \mu m$  (sector X) throughout the ring.  $CWT_{tan}$  increases from  $3.2 \pm 0.3 \mu m$  in sector I to  $3.8 \pm 0.5 \mu m$  in sector VIII and decreases to  $3.3 \pm 0.4 \mu m$  in sector X, whereas  $CWT_{rad}$  increases from  $3.7 \pm 0.4 \mu m$  (I) to  $5.0 \pm 0.5 \mu m$  (X). Consequently,  $CWT_{rad}$  is, on average,  $\sim 0.8 \mu m$  larger than  $CWT_{tan}$ .  $D_{rad}$  displays higher Rbar values than CWT in all sectors. The Rbar values of  $D_{rad}$  and  $CWT_{rad}$  generally increase towards the latewood, while those of  $CWT_{tan}$  remain relatively stable throughout the ring (Table S1). AC1 values of CWT (0.43–0.67) are overall higher than those of  $D_{rad}$  (0.23–0.44).

PCA on the 30 sector chronologies and the six annually resolved TRW, MXD, and TRSI records reveals close similarities in interannual variability between the final three CWT sectors (VIII–X) and MXD,  $\delta^{18}O_c$ ,  $\delta^{13}C_c$ , and  $\delta^{13}C_m$ , as well as between the initial  $D_{rad}$  sectors (I–II) and TRW, and the subsequent  $D_{rad}$  sectors (III–X) and  $\delta^2H_m$  (Fig. 6b). The first three components (PC1–3) explain 69% of the variance and are significant according to the Rnd-Lambda stopping rule (Table S2). PC1 separates  $D_{rad}$  from CWT. The CWT sectors show a smooth transition along PC2 and PC3, while PC3 primarily separates the  $D_{rad}$  sectors.

Correlations between the  $D_{rad}$  sectors and climate data support the results obtained from the annually resolved  $D_{rad}$  record, indicating precipitation as the dominant climatic factor for radial cell expansion (Fig. 6c).  $D_{rad}$  displays significant ( $p < 0.01$ ) correlations with JJA precipitation across all sectors, with  $r$  ranging from 0.38 (I) to 0.54 (IX) for the 30SP data (1931–2020 CE). Although  $D_{rad}$  lacks significant correlation with August precipitation ( $p > 0.01$ ), the scores for June–August are consistently higher than for June–July in all sectors and for all detrendings. In addition, all  $D_{rad}$  sectors indicate significant positive correlations with JJA cloud cover ( $r = 0.32$ – $0.71$ ), particularly prominent in the final three sectors ( $r_{VIII-X} \geq 0.60$ ). The strong  $D_{rad}$  response to JJA cloud cover in sectors VIII–X coincides with the pronounced sensitivity of these data to August  $T_{mean}$  ( $r \geq 0.42$ ; Fig. S11) and the strong negative relationship between August  $T_{mean}$  and cloud cover ( $r = -0.67$ ). For comparison, in June and July, both climate variables are

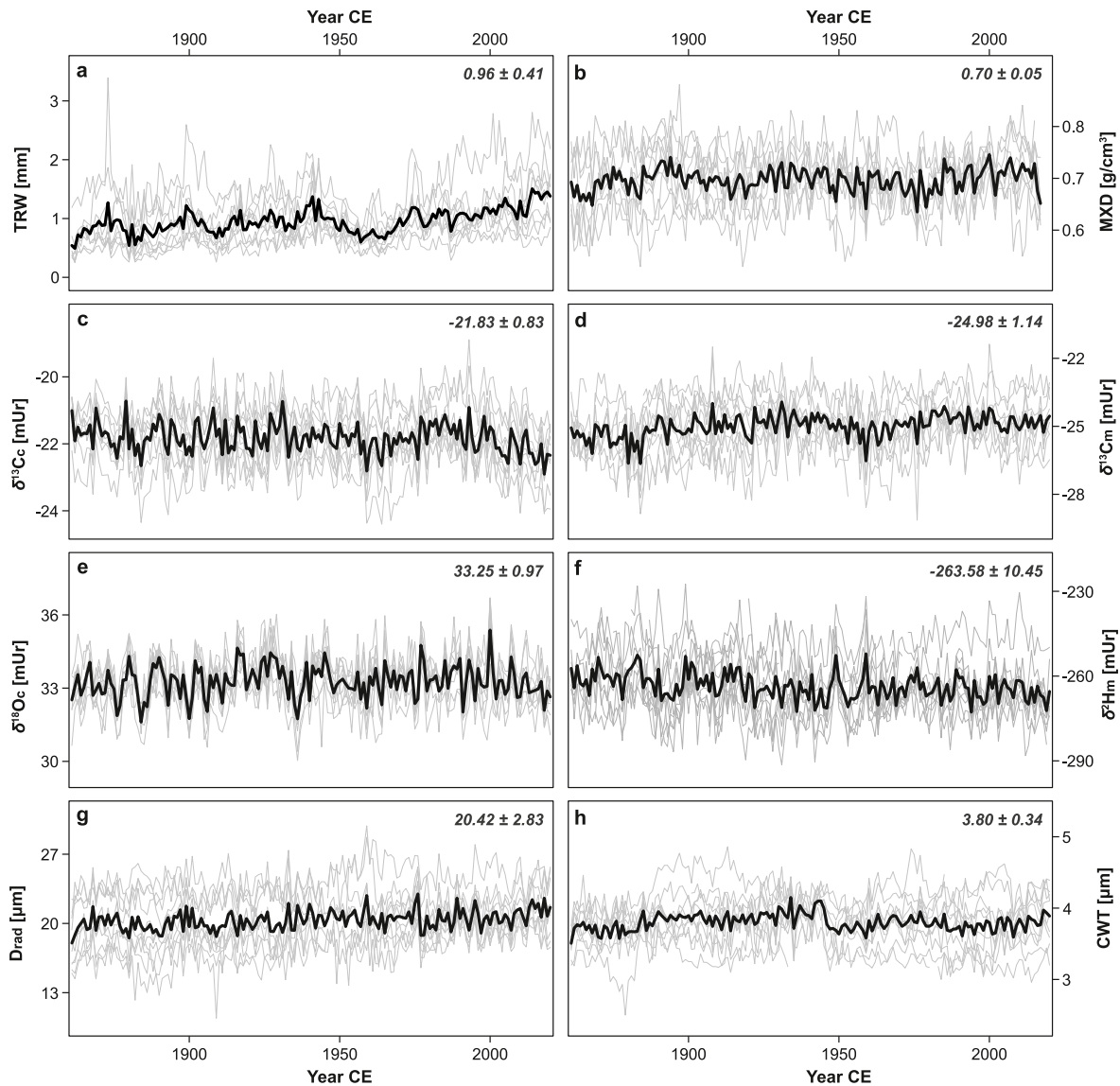


**Fig. 3.** Individual series (grey curves) and mean chronologies (black curves) of raw (a) TRW, (b) MXD, (c)  $\delta^{13}C_c$ , (d)  $\delta^{13}C_m$ , (e)  $\delta^{18}O_c$ , (f)  $\delta^2H_m$ , (g)  $D_{rad}$ , (h) and CWT. The latter represents the mean of  $CWT_{rad}$  and  $CWT_{tan}$  (details in Fig. S4). The  $\delta^{13}C$  series are corrected for the Suess effect. Values at the right top are the arithmetic mean  $\pm 1$  standard deviation calculated over all tree rings between 1861 and 2020 CE (1861–2017 CE for MXD).

**Table 2**  
Correlations between the spline-detrended proxy chronologies for 1861–2020 CE.

	TRW	MXD	$\delta^{13}C_c$	$\delta^{13}C_m$	$\delta^{18}O_c$	$\delta^2H_m$	$D_{rad}$	$CWT_{rad}$	$CWT_{tan}$
TRW									
MXD	0.15								
$\delta^{13}C_c$	0.03	0.45							
$\delta^{13}C_m$	0.27	0.44	0.81						
$\delta^{18}O_c$	-0.04	0.37	0.57	0.42					
$\delta^2H_m$	0.05	-0.40	-0.20	-0.17	-0.06				
$D_{rad}$	0.38	-0.38	-0.55	-0.27	-0.49	0.25			
$CWT_{rad}$	0.11	0.38	0.12	0.12	0.28	-0.29	-0.41		
$CWT_{tan}$	0.48	0.30	-0.12	0.03	0.09	-0.18	0.13	0.70	

**Note:** Values in the left bottom are correlations between the 100SP chronologies, values in the right top are correlations between the 30SP chronologies. Bold numbers indicate significance ( $p < 0.001$ ). Correlations with MXD are computed for 1861–2017 CE.

notably less correlated ( $r = -0.45$  and  $-0.38$ ).

The sectorial CWT chronologies show the strongest climatic response to  $T_{mean}$ , particularly in sectors VIII-X. The highest correlations are found between  $CWT_{rad}$  sectors VIII-X and JJAS  $T_{mean}$  ( $r = 0.46-0.57$ ,  $p < 0.01$  for the 30SP data). The equivalent  $CWT_{tan}$  sectors correlate

substantially weaker with JJAS  $T_{mean}$  ( $r = 0.24-0.34$ ), suggesting a stronger temperature response in  $CWT_{rad}$  compared to  $CWT_{tan}$ . Combining the final three  $CWT_{rad}$  sectors (VIII-X) into one mean chronology representing the latewood ( $CWT_{rad,LW}$ ) results in a 30SP correlation of  $r = 0.55$  with JJAS  $T_{mean}$  ( $p < 0.001$ ). The  $CWT_{rad,LW}$  record

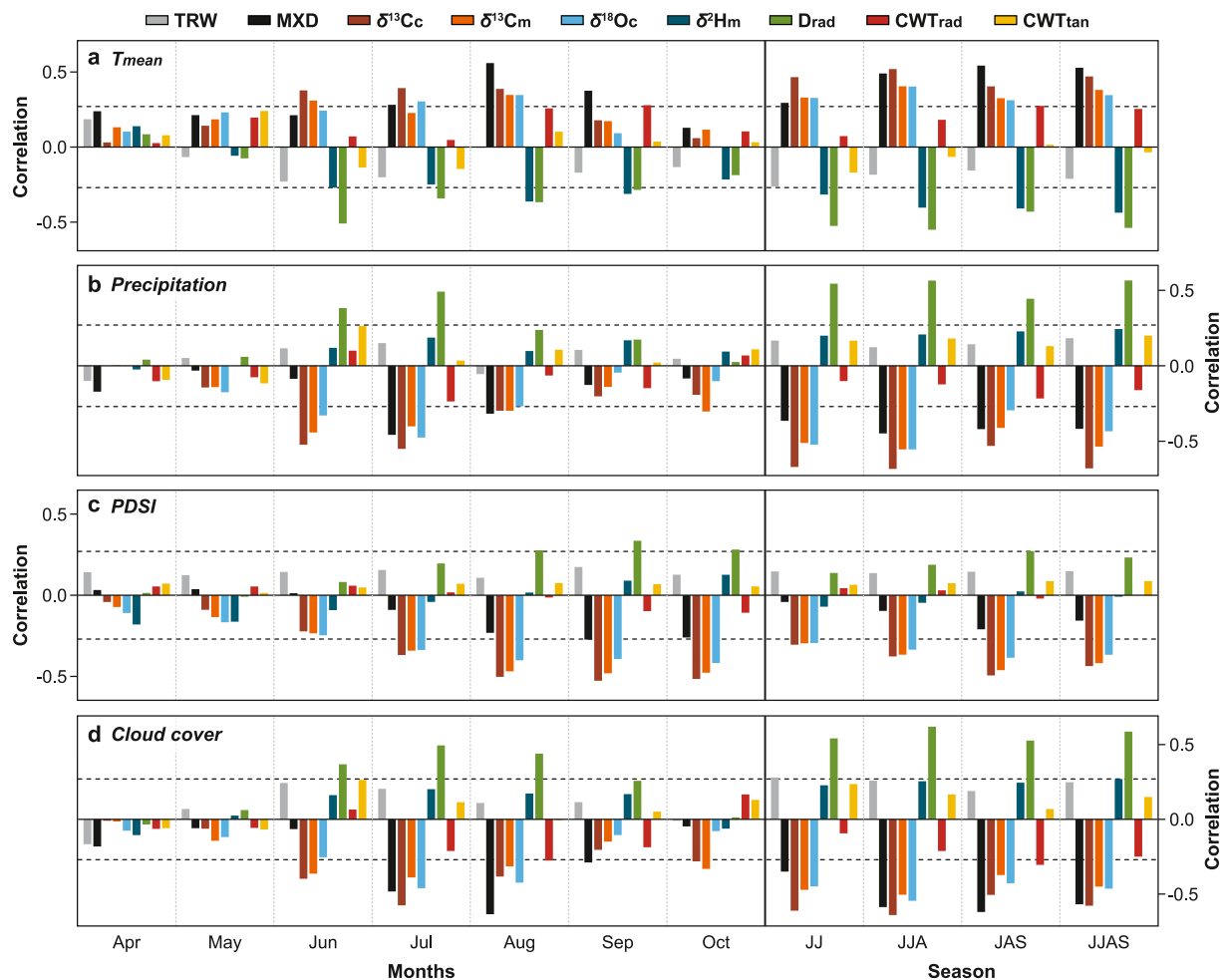


Fig. 4. Climate signals. Correlations between the 30SP-detrended chronologies and monthly/seasonal (a) mean air temperature ( $T_{\text{mean}}$ ), (b) precipitation, (c) the PDSI, and (d) cloud cover data calculated for 1931–2020 CE. Horizontal dashed lines indicate the significance level of  $p < 0.01$ . Please note that the significance level for MXD is marginally higher ( $\sim 0.004$ ) due to the shorter calibration period (1931–2017 CE), but is not displayed for the sake of clarity.

covaries with  $T_{\text{mean}}$  at interannual to decadal scales (2–10 years) but exhibits inconsistencies at lower frequencies (Fig. S8c).

## 4. Discussion

### 4.1. Proxy characteristics and covariance

Among the Mt. Smolikas proxies, cellulose stable carbon and oxygen isotope ratios show the highest inter-series correlations. The strong  $\delta^{13}\text{C}_c$  and  $\delta^{18}\text{O}_c$  coherence is particularly reflected in the high-frequency domain ( $R_{\text{bar}} \geq 0.62$  for the 30SP data) but is also evident in closely aligned low-frequency trends among the individual series (Fig. 3). This finding is in line with previous studies on Mt. Smolikas relict wood (Römer et al., 2023) and living Bosnian pines from the Dinaric Alps (Lukač et al., 2021). Methoxy isotopes show less agreement among the series, with  $R_{\text{bar}}$  values ranging from 0.30 to 0.40, which are similar to those reported for *Larix decidua* from the Western Alps (Riechelmann et al., 2016, 2017) and *Fagus sylvatica* from southern Germany (Anhäuser et al., 2020; Wieland et al., 2022).

Despite lignin methoxy groups exhibiting an average  $^{13}\text{C}$  depletion of 3.15 mUr compared to cellulose, which is consistent with estimates between cellulose and lignin  $\delta^{13}\text{C}$  (Loader et al., 2003; Robertson et al., 2004; Wilson and Grinstead, 1977), the  $\delta^{13}\text{C}$  records of both plant compounds show significant coherence at interannual to decadal timescales ( $\sim 2$ –20 years; Fig. S12a), indicating that these proxies capture similar environmental signals. The lack of lower-frequency covariance ( $>20$

years) partially results from opposing multi-decadal trends, which are particularly evident before 1910 CE and after 2000 CE, but weaken when the  $\delta^{13}\text{C}_c$  data is pin-corrected (McCarroll et al., 2009; Fig. S13).

The anatomical trait profiles of *Pinus heldreichii* closely resemble those of other pine species in central and southern Europe (Carrer et al., 2018; Cuny et al., 2014; Hetzer et al., 2014). The gradual decline in  $D_{\text{rad}}$  from early-to latewood agrees well with that of *Pinus nigra* from Corsica (Hetzer et al., 2014), but is noticeably stronger due to the formation of smaller latewood cells ( $6.7 \pm 1.5 \mu\text{m}$  in sector X). CWT shows a monotonic increase towards latewood, marked by a decline in the final sector, which is more pronounced in  $\text{CWT}_{\text{tan}}$  than  $\text{CWT}_{\text{rad}}$ . The CWT increase in the earlywood and decline in the final latewood portion are characteristic for most conifer species (Babushkina et al., 2024; Cuny et al., 2014; Zharkov et al., 2022; Ziaco et al., 2014). The  $\text{CWT}_{\text{tan}}$  values of *Pinus heldreichii* are similar to those reported for *Pinus cembra* growing at the upper treeline in the Alps ( $\sim 2100$  m a.s.l.), while  $\text{CWT}_{\text{rad}}$  values are, on average,  $\sim 0.7 \mu\text{m}$  higher at Mt. Smolikas (Carrer et al., 2018).

The  $R_{\text{bar}}$  values of the  $D_{\text{rad}}$  sector chronologies, ranging from  $r = 0.25$  to 0.40 after the 30SP detrending, are consistently higher than those of  $\text{CWT}_{\text{rad}}$  and  $\text{CWT}_{\text{tan}}$ . The highest  $R_{\text{bar}}$  value for  $D_{\text{rad}}$  is found at annual resolution ( $r = 0.43$ ), indicating that intra-ring partitioning does not enhance the covariance among the individual series. A similar pattern is observed in  $\text{CWT}_{\text{tan}}$ . However,  $\text{CWT}_{\text{rad}}$  sectors VIII–X exhibit notably higher  $R_{\text{bar}}$  values ( $\geq 0.25$  for the 30SP data) than the annual record, suggesting a stronger climatic signal in latewood CWT. The obtained  $R_{\text{bar}}$  values of the last  $\text{CWT}_{\text{rad}}$  sectors VIII–X are similar to

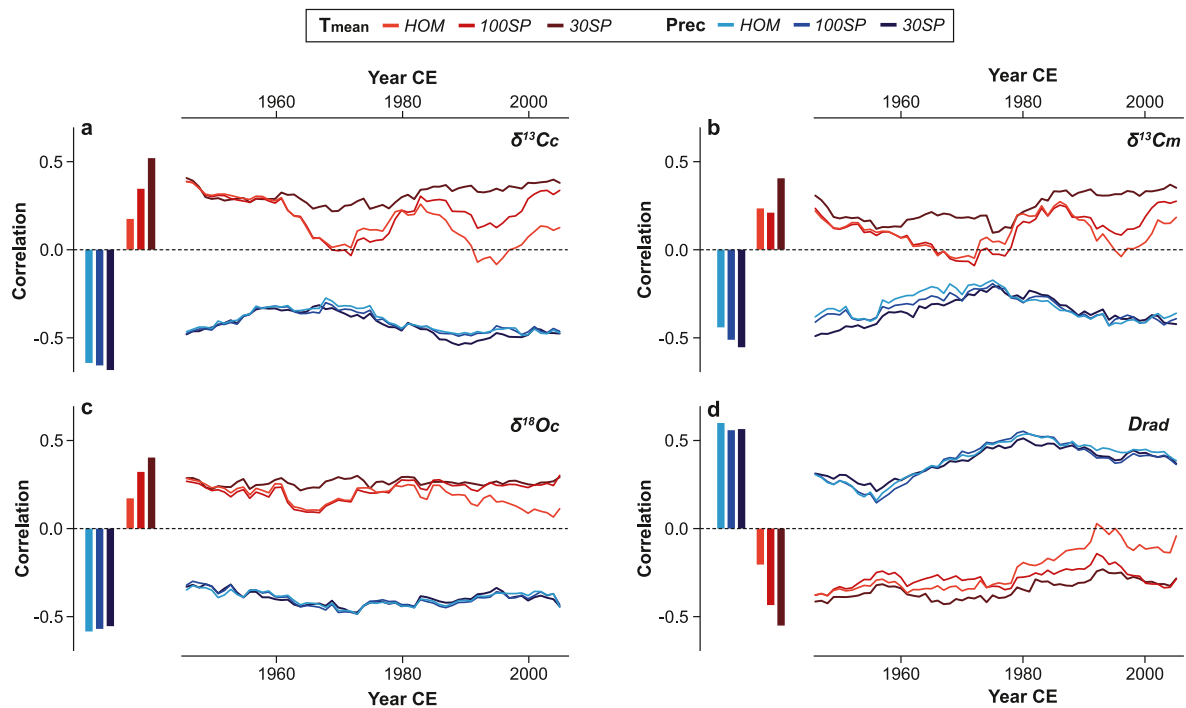


**Fig. 5.** Temporal stability of the temperature ( $T_{\text{mean}}$ ) and precipitation (Prec) signals in  $\delta^{13}\text{C}_c$ ,  $\delta^{13}\text{C}_m$ ,  $\delta^{18}\text{O}_c$ , and  $D_{\text{rad}}$ . Vertical bars (left panels) show correlations between the HOM, 30SP, and 100SP proxy records and June–August  $T_{\text{mean}}$  (red colors) and precipitation (blue colors) calculated for 1931–2020 CE. The curves in the right panels show the corresponding 31-year running correlations for the different detrendings. (For interpretation of the references to color in this figure legend, the reader is referred to the Web version of this article.)

those of MXD (Esper et al., 2020a, 2020b; Römer et al., 2021) and latewood CWT at other high-elevation southern European pine sites (Carrer et al., 2018; Lopez-Saez et al., 2023; Stirbu et al., 2022).

The high AC1 values of TRW and CWT ( $\geq 0.6$ ), particularly evident in the earlywood sectors (Table S1), likely reflect carry-over effects resulting from remobilized photoassimilates during earlywood formation (Kagawa et al., 2006) and indicate greater biological memory effects in TRW and CWT compared to the other proxies (Esper et al., 2015b).  $D_{\text{rad}}$  exhibits lower AC1 values than CWT in all sectors, with higher first-order autocorrelations in the earlywood than in the latewood. Low AC1 values in  $\delta^{13}\text{C}_c$ ,  $\delta^{13}\text{C}_m$ ,  $\delta^{18}\text{O}_c$ , and  $\delta^2\text{H}_m$  ( $\leq 0.41$ ) point to negligible memory effects in the TRSI measurements and are consistent with the fact that the isotopic composition of the samples is not systematically biased by changing earlywood-latewood proportions (Torbenson et al., 2023).

#### 4.2. Climate signals in TRW and MXD

TRW and MXD measurements on Bosnian pines from Mt. Smolikas have proven to be valuable hydroclimate (Esper et al., 2021; Klippel et al., 2018) and temperature proxies (Esper et al., 2020a; Klippel et al., 2019). However, while the observed temperature sensitivity in MXD agrees well with previous studies in terms of seasonality and correlation (Esper et al., 2020a; Klippel et al., 2019), the lack of significant hydroclimate signals in TRW is striking (Esper et al., 2021; Klippel et al., 2018). Although the updated TRW chronology shares more than 72% of variance with the well-replicated ( $n = 872$  series) and precipitation-sensitive TRW record of Esper et al. (2021) from 1861 to 2016 CE, TRW correlations with climate are weak and significant only with diurnal temperature range and summer cloud cover data (Fig. 7a). The lack of significant precipitation correlations can be attributed to the fading sensitivity in the early and mid-20th century, likely related to the limited number of nearby precipitation stations included in the CRU data (Esper et al., 2021; Klippel et al., 2018).

For MXD, we found significant correlations with late-summer

(July–September) temperature, precipitation, and cloud cover. Given the weak correlation between temperature and precipitation in July–September ( $r_{\text{JAS}} = -0.19$ ,  $p > 0.05$ ), the observed responses indicate that *Pinus heldreichii* reacts to both elevated temperatures and low water availability with the formation of denser latewood (Cook et al., 2015; Leonelli et al., 2017). Summer temperature, however, is the dominant climatic driver of MXD (Fig. 7b). The strong cloud-cover correlations reflect the significant dependence of summer precipitation and temperature on cloud coverage ( $r_{\text{JAS}} = 0.56$  and  $-0.52$ ,  $p < 0.001$ ), which can significantly modulate solar radiation fluxes, evapotranspiration processes, and rainfall patterns at the surface level (Geiger et al., 2009).

#### 4.3. Climate signals in stable isotopes

Stable carbon and oxygen isotopes from  $\alpha$ -cellulose and lignin methoxy groups reflect significant temperature and hydroclimatic signals that support previous findings from the Mediterranean region (An et al., 2023; Andreu et al., 2008; Konter et al., 2014; Levanič et al., 2020; Lukač et al., 2021; Szymczak et al., 2012; Treydte et al., 2007). The positive  $\delta^{13}\text{C}$  correlation with summer temperature and negative correlation with summer precipitation appear physiologically meaningful, as high air temperatures and vapor-pressure deficits (VPD) impair  $\text{CO}_2$  diffusion into the needles by stomatal closure, thereby reducing internal  $\text{CO}_2$  concentrations and carboxylation discrimination against  $^{13}\text{C}$ , leading to higher  $\delta^{13}\text{C}$  values (Farquhar et al., 1982). Precipitation events, on the other hand, reduce VPD and allow stomata to open. Moreover, high temperatures and low humidity increase transpiration, which leads to a loss of lighter oxygen isotopes ( $^{16}\text{O}$ ) at the leaf level and thus to higher  $\delta^{18}\text{O}$  values than those of the source water (McCarroll and Loader, 2004). Hence, both  $\delta^{13}\text{C}$  and  $\delta^{18}\text{O}$  are closely linked to summer temperature and moisture conditions, as reflected in the strong correlations of  $\delta^{13}\text{C}_c$ ,  $\delta^{13}\text{C}_m$ , and  $\delta^{18}\text{O}_c$  with these climate variables.

Higher and more robust correlations with June–August precipitation than with air temperature suggest that summer precipitation is the

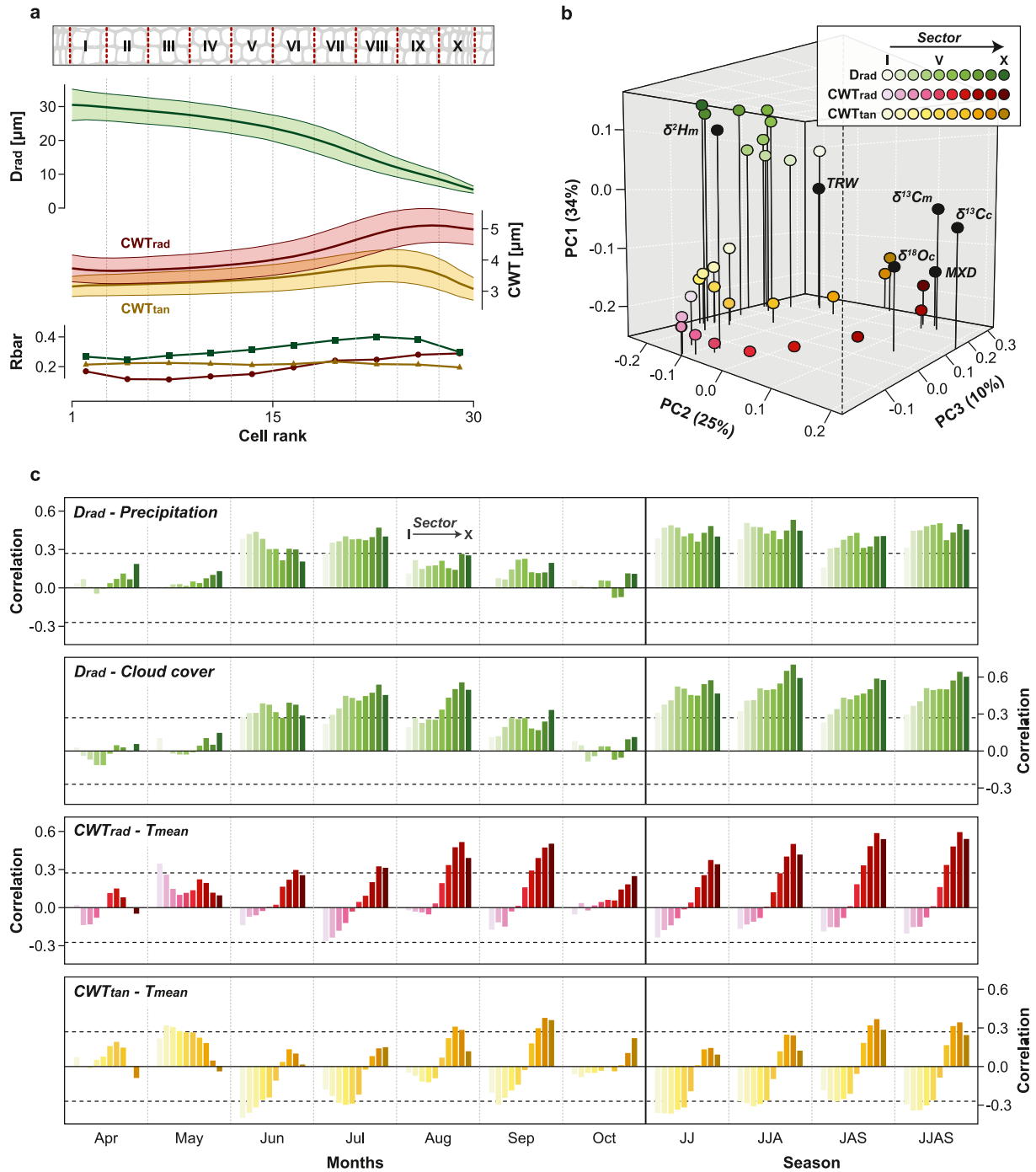


**Fig. 6.** Intra-ring sectors of wood anatomical traits. **(a)** Tracheidograms of  $D_{rad}$  (upper panel),  $CWT_{rad}$ , and  $CWT_{tan}$  (middle panel), shown together with the mean  $Rbar$  of each 30SP sector chronology calculated for 1861–2020 CE (bottom panel). Shaded areas indicate  $\pm 1\sigma$ . The sectors are labeled with Roman numerals (I–X). **(b)** Three-dimensional PCA plot showing the first three principal components computed on the 30SP-detrended TRW, MXD,  $\delta^{13}C_c$ ,  $\delta^{13}C_m$ ,  $\delta^{18}O_c$ ,  $\delta^2H_m$  (black circles) records, and the 30  $D_{rad}$ ,  $CWT_{rad}$ , and  $CWT_{tan}$  sector chronologies (colored circles). **(c)** Correlations between the anatomical sector chronologies (I = left, X = right) and their main climate targets for 1861–2020 CE. Horizontal dashed lines indicate the significance level of  $p < 0.01$ .

dominant climatic forcing of  $\delta^{13}C$  and  $\delta^{18}O$  variability (Fig. 7c–e). This conclusion is supported by significant correlations between  $\delta^{18}O_c$  and the  $\delta^{18}O$  of precipitation (Fig. S14), revealing that  $\delta^{18}O_c$  reflects the  $\delta^{18}O$  signature of the precipitation-derived source water, but is modulated by soil evaporation and transpiration-induced  $^{18}O$  enrichment (Yakir and Sternberg, 2000). The lack of significant correlations with previous-year climate and the low AC1 values of  $\delta^{18}O_c$  indicate that the water used for photosynthetic carbohydrate formation primarily originates from recent precipitation events. Correlations with precipitation are robust over

time and for all detrendings, suggesting that both  $\delta^{13}C$  and  $\delta^{18}O$  reliably reflect summer moisture variations at interannual to multidecadal timescales. Only  $\delta^{13}C_m$  reveals a weaker association at lower frequencies. The robust precipitation signals and the fading temperature sensitivities towards present, particularly evident at lower frequencies (i.e. after the HOM detrending), support previous results on *Pinus hel-dreichii*  $\delta^{13}C_c$  and  $\delta^{18}O_c$  from the Dinaric Alps in Montenegro (Levanić et al., 2020; Lukač et al., 2021), the Apennines in Italy and the Pirin Mountains in Bulgaria (Freund et al., 2023; Treydte et al., 2007).

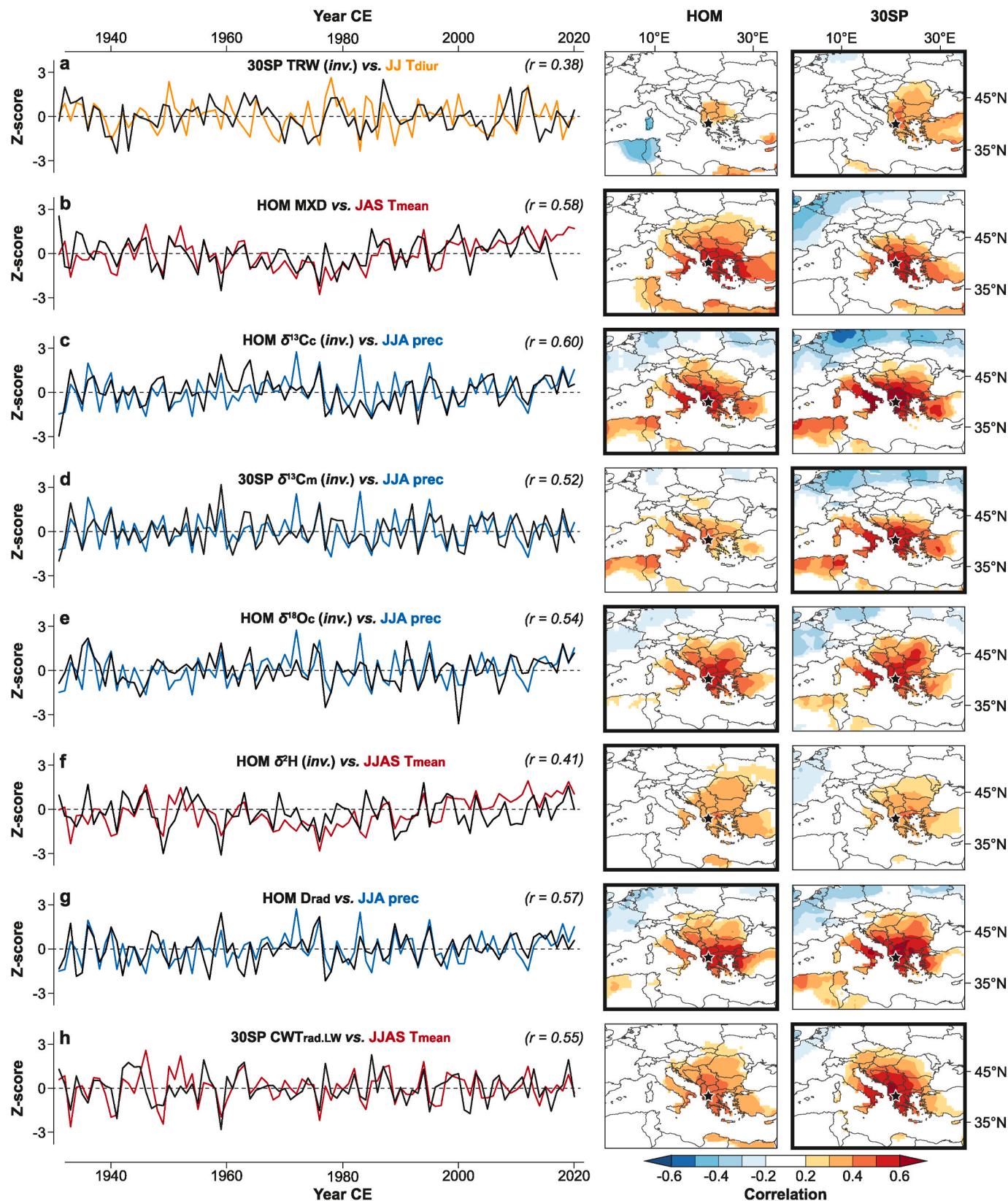


Fig. 7. Best-fit climate targets. Horizontal-mean (HOM) or 30-year-spline (30SP) detrended proxy chronologies (black curves), shown alongside the best-correlated climate records (colored curves). All records are z-transformed. TRW,  $\delta^{13}C_c$ ,  $\delta^{13}C_m$ ,  $\delta^{18}O_c$ , and  $\delta^2H_m$  are inverted. R values indicate the corresponding correlations between the tree-ring and climate data for 1931–2020 CE (2017 CE for MXD). Right panels display field correlations ( $p < 0.05$ ) between the HOM and 30SP-detrended proxies and their climate targets (CRU TS4.07). Thick frames highlight the best fitting frequency (HOM data is preferred). Black stars mark the study site.

Unlike carbon and oxygen isotopes,  $\delta^2\text{H}_m$  is negatively correlated with June–September temperature ( $p < 0.01$ ). Given the lack of studies assessing the climate sensitivity of  $\delta^2\text{H}_m$  in similar environments, our results demonstrate for the first time that  $\delta^2\text{H}_m$  may serve as a reliable temperature proxy in the Mediterranean (Fig. 7f). However, most previous studies reported positive correlations between  $\delta^2\text{H}_m$  and air temperatures at mid-latitudes and lower altitudes (Anhäuser et al., 2020; Lu et al., 2020; Mischel et al., 2015; Wang et al., 2020; Wieland et al., 2022). Only Riechelmann et al. (2017) found a comparable negative temperature response in the  $\delta^2\text{H}_m$  of high-elevation *Larix decidua* trees from the Western Alps. One plausible explanation for this inverse temperature response could be related to the seasonally fluctuating  $\delta^2\text{H}$  signature of precipitation. Since lignin synthesis takes place in the xylem tissue,  $\delta^2\text{H}_m$  is unaffected by the evaporative  $^2\text{H}$  enrichment of leaf water and thus closely reflects the  $\delta^2\text{H}$  signature of the plant's source water, which is positively related to air temperature (Anhäuser et al., 2017). However, similar to findings by Riechelmann et al. (2017), we found a negative correlation between the  $\delta^2\text{H}$  values of methoxy groups and summer rain ( $r_{\text{JJAS}} = -0.27$ ). In summer, the  $\delta^2\text{H}$  values of precipitation are notably higher compared to the other seasons (Fig. S15), resulting in elevated  $\delta^2\text{H}$  values in soil water during years with abundant summer rain and cooler temperatures. Vice versa, in warm and dry summers, the  $\delta^2\text{H}$  values of soil water decrease due to the lower contribution of  $^2\text{H}$ -enriched summer rain. Hence,  $\delta^2\text{H}_m$  seems to reflect the seasonal origin of the source water used for lignin methoxy group formation (Allen et al., 2019). The use of deeper ground water sources may also explain the missing association with precipitation  $\delta^2\text{H}$ , but seems unlikely due to the shallow soils at Mt. Smolikas.

#### 4.4. Climate signals in wood anatomical traits

The wood anatomical features of *Pinus heldreichii* are highly sensitive to hydrothermal conditions in summer.  $D_{\text{rad}}$ , which primarily determines the conductive xylem area, shows a strong summer precipitation response at annual resolution, surpassing that of the sectorial chronologies (Fig. 7g). Greater covariance among the series and stronger climatic responses in  $D_{\text{rad}}$ , compared to tangential diameter and lumen area (not shown), support that climatic imprints are distinctly stronger in the radial than in the tangential lumen diameter (Cuny et al., 2014). The precipitation sensitivity of  $D_{\text{rad}}$  is likely transmitted through soil moisture deficits controlling turgor pressure and cell enlargement (Carvalho et al., 2015; Ziaco, 2020). Abundant rain, on the other hand, promotes the formation of larger tracheid lumina (Fonti et al., 2010; Peters et al., 2021). The precipitation response of  $D_{\text{rad}}$  aligns with studies on western Mediterranean pine species, providing empirical evidence for the importance of summer water availability on conductive xylem properties (Hetzer et al., 2014; Pacheco et al., 2016), and confirms similar hydroclimate signals in *Pinus heldreichii* from high-elevation Eastern Mediterranean sites.

The distinction between  $\text{CWT}_{\text{rad}}$  and  $\text{CWT}_{\text{tan}}$ , along with the intra-ring partitioning, reveal that Bosnian pines primarily respond to high summer temperatures through radial wall thickening of the latewood cells. The final CWT sectors VIII–X show significant positive temperature responses, which are notably stronger in  $\text{CWT}_{\text{rad}}$  than in  $\text{CWT}_{\text{tan}}$ . These results are supported by the regular displacement of the PCA loadings, suggesting a higher agreement with MXD for latewood  $\text{CWT}_{\text{rad}}$  than for  $\text{CWT}_{\text{tan}}$ . The latewood  $\text{CWT}_{\text{rad}}$  record is positively correlated with MXD ( $r_{1861-2017} = 0.68$ ,  $p < 0.001$  for the 30SP data) and shows a strong temperature signal from June to September (Fig. 7h). The significant temperature sensitivity of latewood CWT and the lack of similar climatic responses in earlywood CWT are in line with studies on *Pinus nigra* (Hetzer et al., 2014), *Picea abies* (Castagneri et al., 2017) and *Larix decidua* (Carrer et al., 2016), but differ from those on *Pinus cembra* growing in the Alps and Carpathians, reporting consistent temperature signals in both earlywood and latewood CWT (Carrer et al., 2018; Lopez-Saez et al., 2023; Stirbu et al., 2022).

#### 4.5. Paleoclimatic skill of the tree-ring proxies

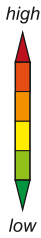
Among all proxies,  $\delta^{13}\text{C}_c$  shows the greatest potential to reconstruct the full spectrum of high-to-low-frequency summer precipitation variability (Fig. 8). The  $\delta^{13}\text{C}_c$  data is characterized by an exceptionally strong covariance among the series and stationary correlations with June–August precipitation throughout the 20th and 21st centuries. The lack of long-term ontogenetic trends in  $\delta^{13}\text{C}_c$  precludes biologically induced low-frequency noise, supporting the use of raw  $\delta^{13}\text{C}_c$  data for climate calibration (Wieland et al., 2024). Given the high inter-series correlation and hydroclimate signal strength ( $r_{\text{RAW}} = 0.63$ ,  $p < 0.001$ , 1931–2020 CE), along with the prolonged climate seasonality compared to TRW (June–July) and the absence of age-related trends, we conclude that annually resolved and non-pooled  $\delta^{13}\text{C}_c$  measurements are a superior proxy to reconstruct past summer precipitation in the Mediterranean, far exceeding the skill of traditional TRW chronologies.

$\delta^{18}\text{O}_c$ ,  $\delta^{13}\text{C}_m$ , and  $D_{\text{rad}}$  also exhibit strong summer precipitation signals. However, these proxies face stronger statistical limitations due to long-term age-related trends in  $\delta^{18}\text{O}_c$  and  $\delta^{13}\text{C}_m$ , and substantial  $\delta^{18}\text{O}_c$  offsets between living and relict wood (Wieland et al., 2024). Significant ontogenetic trends are also characteristic for  $D_{\text{rad}}$ , particularly over the first 100–150 years of tree age (Carrer et al., 2015). Future QWA measurements of relict wood will improve our understanding of such non-climatic noise inherent in anatomical traits. The overlapping precipitation seasonality and strong covariance among  $\delta^{13}\text{C}_c$ ,  $\delta^{18}\text{O}_c$ ,  $\delta^{13}\text{C}_m$ , and  $D_{\text{rad}}$  at interannual to multidecadal timescales, despite minor low-frequency discrepancies in  $\delta^{13}\text{C}_m$ , suggest that proxy combinations could be useful to improve reconstruction skills and assess uncertainties. Moreover, the close association between  $D_{\text{rad}}$  and summer cloud cover, driven by the dependence of precipitation on cloud cover and particularly evident at high frequencies, underscores the potential to gain new insights into past climatic extremes.

MXD shows the greatest potential to reconstruct the full range of interannual to multidecadal summer temperature variability. Although MXD requires standardization prior to chronology development and climate calibration (Bräker, 1981), its stronger temperature sensitivity compared to  $\text{CWT}_{\text{rad,LW}}$  and  $\delta^2\text{H}_m$ , along with its lower workload, highlight MXD's superior paleoclimatic skill in high-elevation Mediterranean environments (Büntgen et al., 2017, 2024; Esper et al., 2020a, 2020b). While latewood  $\text{CWT}_{\text{rad}}$  lacks significant correlation with observational temperatures at decadal to multidecadal scales and can therefore only provide valuable information on past temperature extremes,  $\delta^2\text{H}_m$  can be considered an alternative temperature proxy to MXD. However, further research is needed to consolidate the inverse temperature response of  $\delta^2\text{H}_m$  in the Mediterranean region and to assess signals strengths at lower elevations (Feakins et al., 2013; Greule et al., 2021), where MXD typically fails as a climate proxy.

## 5. Conclusion

Our assessment of covariance and climate signals in TRW, MXD,  $\delta^{13}\text{C}_c$ ,  $\delta^{18}\text{O}_c$ ,  $\delta^{13}\text{C}_m$ ,  $\delta^2\text{H}_m$ ,  $D_{\text{rad}}$ , and CTW from Mt. Smolikas (Greece) reveals advantages of TRSI and QWA measurements over traditional TRW for reconstructing past hydroclimate variability, thereby opening new avenues for an enhanced understanding of past climate dynamics in the Mediterranean over the Common Era (Anchukaitis et al., 2024; Cook et al., 2015). Among all proxies,  $\delta^{13}\text{C}_c$  exhibits the greatest potential for an inter-regional summer precipitation reconstruction, which would be key to contextualize the recent aridification of the Mediterranean. MXD proves to be the most skilful summer temperature proxy, driven by temperature-induced reductions in  $D_{\text{rad}}$  and increases in CWT, especially in August and September. However, while the temperature signals of the anatomical traits alone do not surpass those of MXD,  $\delta^2\text{H}_m$  measurements appear as alternative temperature proxy, potentially capable of capturing climate signals in lower-elevation regions where MXD typically fails as a climate predictor.

8. Workload								References (1) Esper et al. 2021 (2) Esper et al. 2020a (3) Wieland et al. 2024	
7. Detrending									
6. Covariance									
5. Stationarity									
4. Correlation									
3. Frequency									
2. Seasonality									
1. Climate signal									
TRW	T <sub>diur</sub>	JJ	high	-0.38	no	0.32	required <sup>(1)</sup>	●	
MXD	T <sub>mean</sub>	JAS	full	0.58	yes	0.26	required <sup>(2)</sup>	●	
δ <sup>13</sup> C <sub>c</sub>	Precipitation	JJA	full	-0.60	yes	0.56	no <sup>(3)</sup>	●	
δ <sup>13</sup> C <sub>m</sub>	Precipitation	JJA	high	-0.52	yes	0.30	required <sup>(3)</sup>	●	
δ <sup>18</sup> O <sub>c</sub>	Precipitation	JJA	full	-0.54	yes	0.55	required <sup>(3)</sup>	●	
δ <sup>2</sup> H <sub>m</sub>	T <sub>mean</sub>	JJAS	full	-0.41	yes	0.24	required <sup>(3)</sup>	●	
Drad	Precipitation	JJA	full	0.57	yes	0.29	likely required	●	
CWTrad.LW	T <sub>mean</sub>	JJAS	high	0.55	yes	0.36	likely required	●	

**Fig. 8.** Paleoclimatic potential of the tree-ring proxies. Summary of the best-fit climate calibrations computed for 1931–2020 CE (1931–2017 CE for MXD). Please note that correlation and covariance values refer to the optimum frequency (high = 30SP data, full = HOM data) and may deviate slightly from the values in Table 1 due to the shorter period.

#### Author contributions

P.R., A.W., F.K., and J.E. conceived and designed the study. P.R., A.W., and F.K. collected the samples. P.R. and A.W. prepared the samples for isotope analyses. O.U., J.C., and N.P. measured the stable isotope ratios of cellulose, A.W. and M.G. measured the stable isotope ratios of lignin methoxy groups. P.R. and E.Z. produced the wood anatomical data. P.R. and A.W. performed data analyses and drafted the manuscript with input from M.C.A.T., F.R., E.Z., D.F., M.G., O.U., J.C., N.P., M.T., M.C., U.B., F.K., and J.E. All authors provided discussion and agreed to the final version of the manuscript.

#### Declaration of competing interest

The authors declare that they have no known competing financial interests or personal relationships that could have appeared to influence the work reported in this paper.

#### Acknowledgements

We thank Tilmann Büttner, Zuzana Černá, Manuel Dienst, Yannik Esser, Katharina Hechler, Nora Jubelius, Lisa Kinder, Lennart Klein, Lara Klippel, Bernd Knape, Oliver Konter, Markus Kochbeck, Stephanie Kühmichel, Paul Krusic, Inna Roshka, Luzie Schneider, Philipp Schulz, Katharina Vinnen, and Heike Zimmer-Zachmann for field and laboratory work. Supported by the German Research Foundation (Grant No. ES 161/12-1 and KE 884/17-1), the European Union (ERC Advanced grant MONOSTAR, Grant No. 882727 and ERC Synergy-Grant Synergy-Plague, Grant No. 101118880), the Czech Science Foundation (HYDRO8, Grant No. 23–08049 S), and the Ministry of Education, Youth and Sports of the Czech Republic (AdAgriF; Grant No. CZ.02.01.01/00/22\_008/0004635).

#### Appendix A. Supplementary data

Supplementary data to this article can be found online at <https://doi.org/10.1016/j.quascirev.2025.109270>.

[org/10.1016/j.quascirev.2025.109270](https://doi.org/10.1016/j.quascirev.2025.109270).

#### Data availability

A link to the data and/or code is provided as part of this submission.

#### References

- Allen, S.T., Kirchner, J.W., Braun, S., Siegwolf, R.T.W., Goldsmith, G.R., 2019. Seasonal origins of soil water used by trees. *Hydrol. Earth Syst. Sci.* 23, 1199–1210. <https://doi.org/10.5194/hess-23-1199-2019>.
- An, W., Xu, C., Marković, S.B., Sun, Y., Gavrilo, M.B., Govedar, Z., Hao, Q., Guo, Z., 2023. Anthropogenic warming has exacerbated droughts in southern Europe since the 1850s. *Commun. Earth Environ.* 4, 232.
- Anchukaitis, K.J., Touchan, R., Meko, D.M., Kherchouche, D., Slimani, S., Sivrikaya, F., Ilmen, R., Mitsopoulos, I., Stephan, J., Attieh, J., et al., 2024. Enhancing spatiotemporal paleoclimate reconstructions of hydroclimate across the Mediterranean over the last millennium. *Clim. Dyn.* <https://doi.org/10.1007/s00382-024-07166-6>.
- Andreu, L., Planells, O., Gutierrez, E., Helle, G., Schleser, G.H., 2008. Climatic significance of tree-ring width and δ<sup>13</sup>C in a Spanish pine forest network. *Tellus B: Chem. Phys. Meteorol.* 60, 771–781. <https://doi.org/10.1111/j.1600-0889.2008.00370.x>.
- Anhäuser, T., Greule, M., Polag, D., Bowen, G.J., Keppler, F., 2017. Mean annual temperatures of mid-latitude regions derived from δ<sup>2</sup>H values of wood lignin methoxyl groups and its implications for paleoclimate studies. *Sci. Total Environ.* 574, 1276–1282. <https://doi.org/10.1016/j.scitotenv.2016.07.189>.
- Anhäuser, T., Sehls, B., Thomas, W., Hartl, C., Greule, M., Scholz, D., Esper, J., Keppler, F., 2020. Tree-ring δ<sup>2</sup>H values from lignin methoxyl groups indicate sensitivity to European scale temperature changes. *Palaeogeogr. Palaeoclimatol. Palaeoecol.* 546, 109665. <https://doi.org/10.1016/j.palaeo.2020.109665>.
- Babushkina, E.A., Dergunov, D.R., Zharkov, M.S., Belokopytova, L.V., Zhirnova, D.F., Yang, B., Liu, J., Peng, X., Vaganov, E.A., 2024. Wood anatomy chronologies of Scots pine in the foothills of the Western Sayan (Siberia). *J. For. Res.* 35, 45. <https://doi.org/10.1007/s11676-023-01692-5>.
- Balanzategui, D., Nordhauß, H., Heinrich, I., Biondi, F., Miley, N., Hurley, A.G., Ziaco, E., 2021. Wood anatomy of Douglas-fir in eastern Arizona and its relationship with Pacific Basin climate. *Front. Plant Sci.* 12, 702442. <https://doi.org/10.3389/fpls.2021.702442>.
- Belmecheri, S., Wright, W.E., Szejner, P., 2022. Sample collection and preparation for annual and intra-annual tree-ring isotope chronologies. In: Siegwolf, R.T.W., Brooks, J.R., Roden, J., Saurer, M. (Eds.), *Stable Isotopes in Tree Rings – Inferring Physiological, Climatic and Environmental Responses*. Springer, Cham, pp. 103–134.
- Belokopytova, L.V., Babushkina, E.A., Zhirnova, D.F., Panyushkina, I.P., Vaganov, E.A., 2019. Pine and larch tracheids capture seasonal variations of climatic signal at

- moisture-limited sites. *Trees* (Berl.) 33, 227–242. <https://doi.org/10.1007/s00468-018-1772-2>.
- Björklund, J., Seftigen, K., Fonti, P., Nievergelt, D., von Arx, G., 2020. Dendroclimatic potential of dendroanatomy in temperature-sensitive *Pinus sylvestris*. *Dendrochronologia* 60, 125673. <https://doi.org/10.1016/j.dendro.2020.125673>.
- Björklund, J., Seftigen, K., Stoffel, M., Fonti, M.V., Kottlow, S., Frank, D.C., Esper, J., Fonti, P., Gooose, H., Gunnarson, B.E., et al., 2023. Fennoscandian tree-ring anatomy shows a warmer modern than medieval climate. *Nature* 620, 97–103. <https://doi.org/10.1038/s41586-023-06176-4>.
- Boettger, T., Haupt, M., Knöller, K., Weise, S.M., Waterhouse, J.S., Rinne, K.T., Loader, N.J., Sonninen, E., Jungner, H., Masson-Delmotte, V., et al., 2007. Wood cellulose preparation methods and mass spectrometric analyses of  $\delta^{13}\text{C}$ ,  $\delta^{18}\text{O}$ , and nonexchangeable  $\delta^2\text{H}$  values in cellulose, sugar, and starch: an interlaboratory comparison. *Anal. Chem.* 79, 4603–4612. <https://doi.org/10.1021/ac0700023>.
- Bräker, O.U., 1981. Der Alterstrend bei Jahrringdichten und Jahrringbreiten von Nadelhölzern und sein Ausgleich. *Mitt. Forstl. Bundesversuchsanst. Wien* 142, 75–102.
- Brand, W.A., Coplen, T.B., 2012. Stable isotope deltas: tiny, yet robust signatures in nature. *Isot. Environ. Health Stud.* 48, 393–409. <https://doi.org/10.1080/10256016.2012.666977>.
- Büntgen, U., 2022. Scrutinizing tree-ring parameters for Holocene climate reconstructions. *WIREs Clim. Change* 13, e778. <https://doi.org/10.1002/wcc.778>.
- Büntgen, U., Krusic, P.J., Verstege, A., Sangüesa-Barreda, G., Wagner, S., Camarero, J.J., Ljungqvist, F.C., Zorita, E., Oppenheimer, C., Konter, O., et al., 2017. New tree-ring evidence from the Pyrenees reveals Western Mediterranean climate variability since medieval times. *J. Clim.* 30, 5295–5318. <https://doi.org/10.1175/JCLI-D-16-0526.1>.
- Büntgen, U., Kolár, T., Rybníček, M., Koňasová, E., Trnka, M., Ač, A., Krusic, P.J., Esper, J., Treydte, K., Reinig, F., Kirilyanov, A., Herzog, F., Urban, O., 2020. No age trends in stable isotopes. *Paleoceanogr. Paleoclimatol.* 35, e2019PA003831. <https://doi.org/10.1029/2019PA003831>.
- Büntgen, U., Urban, O., Krusic, P.J., Rybníček, M., Kolár, T., Kyncl, T., Ač, A., Koňasová, E., Časlavský, J., Esper, J., et al., 2021. Recent European drought extremes beyond Common Era background variability. *Nat. Geosci.* 14, 190–196. <https://doi.org/10.1038/s41561-021-00698-0>.
- Büntgen, U., Reinig, F., Verstege, A., Piermattei, A., Kunz, M., Krusic, P.J., Slavin, P., Stépánek, P., Torbenson, M., Martínez del Castillo, E., et al., 2024. Recent summer warming over the western Mediterranean region is unprecedented since medieval times. *Glob. Planet. Change* 232, 104336. <https://doi.org/10.1016/j.gloplacha.2023.104336>.
- Carrer, M., von Arx, G., Castagneri, D., Petit, G., 2015. Distilling allometric and environmental information from time series of conduit size: the standardization issue and its relationship to tree hydraulic architecture. *Tree Physiol.* 35, 27–33. <https://doi.org/10.1093/treephys/tpu108>.
- Carrer, M., Brunetti, M., Castagneri, D., 2016. The imprint of extreme climate events in century-long time series of wood anatomical traits in high-elevation conifers. *Front. Plant Sci.* 7, 683. <https://doi.org/10.3389/fpls.2016.00683>.
- Carrer, M., Unterholzner, L., Castagneri, D., 2018. Wood anatomical traits highlight complex temperature influence on *Pinus cembra* at high elevation in the Eastern Alps. *Int. J. Biometeorol.* 62, 1745–1753. <https://doi.org/10.1007/s00484-018-1577-4>.
- Carvalho, A., Nabais, C., Vieira, J., Rossi, S., Campelo, F., 2015. Plastic response of tracheids in *Pinus pinaster* in a water-limited environment: adjusting lumen size instead of wall thickness. *PLoS One* 10, e0136305. <https://doi.org/10.1371/journal.pone.0136305>.
- Castagneri, D., Fonti, P., von Arx, G., Carrer, M., 2017. How does climate influence xylem morphogenesis over the growing season? Insights from long-term intra-ring anatomy in *Picea abies*. *Ann. Bot.* 119, 1011–1020. <https://doi.org/10.1093/aob/mcw274>.
- Cook, E.R., Peters, K., 1997. Calculating unbiased tree-ring indices for the study of climatic and environmental change. *Holocene* 7, 361–370. <https://doi.org/10.1177/095968369700700314>.
- Cook, E.R., Seager, R., Kushnir, Y., Briffa, K.R., Büntgen, U., Frank, D., Krusic, P.J., Tegel, W., van der Schrier, G., Andreu-Hayles, L., et al., 2015. Old World megadroughts and pluvials during the Common Era. *Sci. Adv.* 1, e1500561. <https://doi.org/10.1126/sciadv.1500561>.
- Cook, E.R., Krusic, P.J., Peters, K., Holmes, R.L., 2017. Program ARSTAN (ARS41d), Autoregressive tree-ring standardization program. Tree-ring laboratory of Lamont-Doherty Earth Observatory, Palisades, NY.
- Cramer, W., Guiot, J., Fader, M., Garrabou, J., Gattuso, J.-P., Iglesias, A., Lange, M.A., Lionello, P., Llasat, M.C., Paz, S., et al., 2018. Climate change and interconnected risks to sustainable development in the Mediterranean. *Nat. Clim. Change* 8, 972–980. <https://doi.org/10.1038/s41558-018-0299-2>.
- Cuny, H.E., Rathgeber, C.B.K., Frank, D.C., Fonti, P., Fourmier, M., 2014. Kinetics of tracheid development explain conifer tree-ring structure. *New Phytol.* 203, 1231–1241. <https://doi.org/10.1111/nph.12871>.
- Dansgaard, W., 1964. Stable isotopes in precipitation. *Tellus A: Dyn. Meteorol. Oceanogr.* 16, 436–468. <https://doi.org/10.3402/tellusa.v16i4.8993>.
- Dorado Liñán, I., Gutiérrez, E., Heinrich, I., Andreu-Hayles, L., Muntán, E., Campelo, F., Helle, G., 2012. Age effects and climate response in trees: a multi-proxy tree-ring test in old-growth life stages. *Eur. J. Forest Res.* 131, 933–944. <https://doi.org/10.1007/s10342-011-0566-5>.
- Esper, J., Konter, O., Krusic, P.J., Saurer, M., Holzkämper, S., Büntgen, U., 2015a. Long-term summer temperature variations in the Pyrenees from detrended stable carbon isotopes. *Geochronometria* 42, 53–59. <https://doi.org/10.1515/geochr-2015-0006>.
- Esper, J., Schneider, L., Smerdon, J.E., Schöne, B.R., Büntgen, U., 2015b. Signals and memory in tree-ring width and density data. *Dendrochronologia* 35, 62–70. <https://doi.org/10.1016/j.dendro.2015.07.001>.
- Esper, J., Klippel, L., Krusic, P.J., Konter, O., Raible, C.C., Xoplaki, E., Luterbacher, J., Büntgen, U., 2020a. Eastern Mediterranean summer temperatures since 730 CE from Mt. Smolikas tree-ring densities. *Clim. Dyn.* 54, 1367–1382. <https://doi.org/10.1007/s00382-019-05063-x>.
- Esper, J., Hartl, C., Tejedor, E., de Luis, M., Günther, B., Büntgen, U., 2020b. High-resolution temperature variability reconstructed from Black pine tree ring densities in southern Spain. *Atmosphere* 11, 748. <https://doi.org/10.3390/atmos11070748>.
- Esper, J., Konter, O., Klippel, L., Krusic, P.J., Büntgen, U., 2021. Pre-instrumental summer precipitation variability in northwestern Greece from a high-elevation *Pinus heldreichii* network. *Int. J. Climatol.* 41, 2828–2839. <https://doi.org/10.1002/joc.6992>.
- Farquhar, G.D., O'Leary, M.H., Berry, J.A., 1982. On the relationship between carbon isotope discrimination and the intercellular carbon dioxide concentration in leaves. *Aust. J. Plant Physiol.* 9, 121–137.
- Feakins, S.J., Ellsworth, P.V., Sternberg, L., 2013. Lignin methoxyl hydrogen isotope ratios in a coastal ecosystem. *Geochim. Cosmochim. Acta* 121, 54–66. <https://doi.org/10.1016/j.gca.2013.07.012>.
- Fonti, P., von Arx, G., García-González, I., Eilmann, B., Sass-Klaassen, U., Gärtner, H., Eckstein, D., 2010. Studying global change through investigation of the plastic responses of xylem anatomy in tree rings. *New Phytol.* 185, 42–53. <https://doi.org/10.1111/j.1469-8137.2009.03030.x>.
- Frank, D.C., Esper, J., Cook, E.R., 2007. Adjustment for proxy number and coherence in a large-scale temperature reconstruction. *Geophys. Res. Lett.* 34, L16709. <https://doi.org/10.1029/2007GL030571>.
- Freund, M.B., Helle, G., Baling, D.F., Ballis, N., Schleser, G.H., Cubasch, U., 2023. European tree-ring isotopes indicate unusual recent hydroclimate. *Commun. Earth Environ.* 4, 26. <https://doi.org/10.1038/s43247-022-00648-7>.
- Gagen, M., McCarroll, D., Loader, N.J., Robertson, I., Jalkanen, R., Anchukaitis, K.J., 2007. Exorcising the 'segment length curse': summer temperature reconstruction since AD 1640 using non-detrended stable carbon isotope ratios from pine trees in northern Finland. *Holocene* 17, 435–446. <https://doi.org/10.1177/0959683607077012>.
- Geiger, R., Aron, R.H., Todhunter, P., 2009. *The Climate Near the Ground*. Rowman & Littlefield Publishing Group, Lanham, MD.
- González-Cásares, M., Camarero, J.J., Colangelo, M., Rita, A., Poma-García, M., 2019. High responsiveness of wood anatomy to water availability and drought near the equatorial rear edge of Douglas-fir. *Can. J. For. Res.* 49, 1114–1123. <https://doi.org/10.1139/cjfr-2019-0120>.
- Gori, Y., Wehrens, R., Greule, M., Keppler, F., Ziller, L., La Porta, N., Camin, F., 2013. Carbon, hydrogen and oxygen stable isotope ratios of whole wood, cellulose and lignin methoxyl groups of *Picea abies* as climate proxies. *Rapid Commun. Mass Spectrom.* 27, 265–275. <https://doi.org/10.1002/rcm.6446>.
- Greule, M., Mosandl, A., Hamilton, J.T.G., Keppler, F., 2008. A rapid and precise method for determination of D/H ratios of plant methoxyl groups. *Rapid Commun. Mass Spectrom.* 22, 3983–3988. <https://doi.org/10.1002/rcm.3817>.
- Greule, M., Mosandl, A., Hamilton, J.T.G., Keppler, F., 2009. A simple rapid method to precisely determine  $^{13}\text{C}/^{12}\text{C}$  ratios of plant methoxyl groups. *Rapid Commun. Mass Spectrom.* 23, 1710–1714. <https://doi.org/10.1002/rcm.4057>.
- Greule, M., Moossen, H., Geilmann, H., Brand, W.A., Keppler, F., 2019. Methyl sulfates as methoxy isotopic reference materials for  $\delta^{13}\text{C}$  and  $\delta^2\text{H}$  measurements. *Rapid Commun. Mass Spectrom.* 33, 343–350. <https://doi.org/10.1002/rcm.8355>.
- Greule, M., Moossen, H., Lloyd, M.K., Geilmann, H., Brand, W.A., Eiler, J.M., Qi, H., Keppler, F., 2020. Three wood isotopic reference materials for  $\delta^2\text{H}$  and  $\delta^{13}\text{C}$  measurements of plant methoxy groups. *Chem. Geol.* 533, 119428. <https://doi.org/10.1016/j.chemgeo.2019.119428>.
- Greule, M., Wieland, A., Keppler, F., 2021. Measurements and applications of  $\delta^2\text{H}$  values of wood lignin methoxy groups for paleoclimatic studies. *Quat. Sci. Rev.* 268, 107107. <https://doi.org/10.1016/j.quascirev.2021.107107>.
- Harris, I., Osborn, T.J., Jones, P., Lister, D., 2020. Version 4 of the CRU TS monthly high-resolution gridded multivariate climate dataset. *Sci. Data* 7, 109. <https://doi.org/10.1038/s41597-020-0453-3>.
- Hartl-Meyrer, C., Zang, C., Büntgen, U., Esper, J., Rothe, A., Göttlein, A., Dirnböck, T., Treydte, K., 2015. Uniform climate sensitivity in tree-ring stable isotopes across species and sites in a mid-latitude temperate forest. *Tree Physiol.* 35, 4–15. <https://doi.org/10.1093/treephys/tpu096>.
- Hetzler, T., Bräuning, A., Leuschner, H.H., 2014. High-resolution climatic analysis of wood anatomical features in Corsican pine from Corsica (France) using latewood tracheid profiles. *Trees* (Berl.) 28, 1279–1288. <https://doi.org/10.1007/s00468-014-1045-7>.
- Hoerling, M., Eischeid, J., Perlwitz, J., Quan, X.W., Zhang, T., Pegion, P., 2012. On the increased frequency of Mediterranean drought. *J. Clim.* 25, 2146–2161. <https://doi.org/10.1175/JCLI-D-11-00296.1>.
- Kagawa, A., Sugimoto, A., Maximov, T.C., 2006.  $^{13}\text{C}$  pulse-labelling of photoassimilates reveals carbon allocation within and between tree rings. *Plant Cell Environ.* 29, 1571–1584. <https://doi.org/10.1111/j.1365-3040.2006.01533.x>.
- Keeling, C.D., 1979. The Suess effect:  $^{13}\text{C}$  Carbon- $^{14}\text{C}$  Carbon interrelations. *Environ. Int.* 2, 229–300. [https://doi.org/10.1016/0160-4120\(79\)90005-9](https://doi.org/10.1016/0160-4120(79)90005-9).
- Keeling, C.D., Piper, S.C., Bacastow, R.B., Wahlen, M., Whorf, T.P., Heimann, M., Meijer, H.A., 2005. Atmospheric  $\text{CO}_2$  and  $^{13}\text{C}$  exchange with the terrestrial biosphere and oceans from 1978 to 2000: observations and carbon cycle implications. In: Baldwin, I.T., Caldwell, M.M., Heldmaier, G., Jackson, R.B., Lange, O.L., Mooney, H.A., Schulze, E.D., Sommer, U., Ehleringer, J.R., Dearing, M.D., et al. (Eds.), *A History of Atmospheric  $\text{CO}_2$  and Its Effects on Plants, Animals, and Ecosystems*. Springer, New York, pp. 83–113.

- Keppler, F., Kalin, R.M., Harper, D.B., McRoberts, W.C., Hamilton, J.T.G., 2004. Carbon isotope anomaly in the major plant C<sub>1</sub> pool and its global biogeochemical implications. *Biogeosciences* 1, 123–131. <https://doi.org/10.5194/bg-1-123-2004>.
- Keppler, F., Harper, D.B., Kalin, R.M., Meier-Augenstein, W., Farmer, N., Davis, S., Schmidt, H.L., Brown, D.M., Hamilton, J.T.G., 2007. Stable hydrogen isotope ratios of lignin methoxyl groups as a paleoclimate proxy and constraint of the geographical origin of wood. *New Phytol.* 176, 600–609. <https://doi.org/10.1111/j.1469-8137.2007.02213.x>.
- Klippel, L., Krusic, P.J., Brandes, R., Hartl, C., Belmecheri, S., Dienst, M., Esper, J., 2018. A 1286-year hydro-climate reconstruction for the Balkan Peninsula. *Boreas* 47, 1218–1229. <https://doi.org/10.1111/bor.12320>.
- Klippel, L., Krusic, P.J., Konter, O., St George, S., Trouet, V., Esper, J., 2019. A 1200+ year reconstruction of temperature extremes for the northeastern Mediterranean region. *Int. J. Climatol.* 39, 2336–2350. <https://doi.org/10.1002/joc.5955>.
- Konter, O., Holzkämper, S., Helle, G., Büntgen, U., Saurer, M., Esper, J., 2014. Climate sensitivity and parameter coherency in annually resolved  $\delta^{13}\text{C}$  and  $\delta^{18}\text{O}$  from *Pinus uncinata* tree-ring data in the Spanish Pyrenees. *Chem. Geol.* 377, 12–19. <https://doi.org/10.1016/j.chemgeo.2014.03.021>.
- Leonelli, G., Coppola, A., Salvatore, M.C., Baroni, C., Battipaglia, G., Gentilesca, T., Ripullone, F., Borghetti, M., Conte, E., Tognetti, R., et al., 2017. Climate signals in a multispecies tree-ring network from central and southern Italy and reconstruction of the late summer temperatures since the early 1700s. *Clim. Past* 13, 1451–1471. <https://doi.org/10.5194/cp-13-1451-2017>.
- Levanic, T., Jevšenak, J., Hafner, P., 2020. Stable isotopes reveal climate signal hidden in tree rings of endemic Balkan pines. *Atmosphere* 11, 135. <https://doi.org/10.3390/atmos11020135>.
- Lionello, P., Scarascia, L., 2018. The relation between climate change in the Mediterranean region and global warming. *Reg. Environ. Change* 18, 1481–1493. <https://doi.org/10.1007/s10113-018-1290-1>.
- Loader, N.J., Robertson, I., McCarroll, D., 2003. Comparison of stable carbon isotope ratios in the whole wood, cellulose and lignin of oak tree-rings. *Palaeogeogr. Palaeoclimatol. Palaeoecol.* 196, 395–407. [https://doi.org/10.1016/S0031-0182\(03\)00466-8](https://doi.org/10.1016/S0031-0182(03)00466-8).
- Lopez-Saez, J., Corona, C., von Arx, G., Fonti, P., Slamova, L., Stoffel, M., 2023. Tree-ring anatomy of *Pinus cembra* trees opens new avenues for climate reconstructions in the European Alps. *Sci. Total Environ.* 855, 158605. <https://doi.org/10.1016/j.scitotenv.2022.158605>.
- Lu, Q., Liu, X., Anhäuser, T., Keppler, F., Wang, Y., Zeng, X., Zhang, Q., Zhang, L., Wang, K., Zhang, Y., 2020. Tree-ring lignin proxies in *Larix gmelinii* forest growing in a permafrost area of northeastern China: temporal variation and potential for climate reconstructions. *Ecol. Indic.* 118, 106750. <https://doi.org/10.1016/j.ecolind.2020.106750>.
- Lukač, L., Mikac, S., Urban, O., Kolář, T., Rybníček, M., Ač, A., Trnka, M., Marek, M.V., 2021. Stable isotopes in tree rings of *Pinus heldreichii* can indicate climate variability over the Eastern Mediterranean region. *Forests* 12, 350. <https://doi.org/10.3390/f12030350>.
- Luterbacher, J., García-Herrera, R., Akcer-On, S., Allan, R., Alvarez-Castro, M.C., Benito, G., Booth, J., Büntgen, U., Cagatay, N., Colombaroli, D., et al., 2012. A review of 2000 years of paleoclimatic evidence in the Mediterranean. In: Lionello, P. (Ed.), *The Climate of the Mediterranean Region: from the Past to the Future*. Elsevier, Amsterdam, pp. 87–185.
- McCarroll, D., Loader, N.J., 2004. Stable isotopes in tree rings. *Quat. Sci. Rev.* 23, 771–801. <https://doi.org/10.1016/j.quascirev.2003.06.017>.
- McCarroll, D., Gagen, M.H., Loader, N.J., Robertson, I., Anchukaitis, K.J., Los, S., Young, G.H.F., Jalkanen, R., Kirchhefer, A., Waterhouse, J.S., 2009. Correction of tree ring stable carbon isotope chronologies for changes in the carbon dioxide content of the atmosphere. *Geochim. Cosmochim. Acta* 73, 1539–1547. <https://doi.org/10.1016/j.gca.2008.11.041>.
- Mischel, M., Esper, J., Keppler, F., Greule, M., Werner, W., 2015.  $\delta^2\text{H}$ ,  $\delta^{13}\text{C}$  and  $\delta^{18}\text{O}$  from whole wood,  $\alpha$ -cellulose and lignin methoxyl groups in *Pinus sylvestris*: a multi-parameter approach. *Isot. Environ. Health Stud.* 51, 553–568. <https://doi.org/10.1080/10256016.2015.1056181>.
- Nakatsuka, T., Sano, M., Li, Z., Xu, C., Tsushima, A., Shigeoka, Y., Sho, K., Ohnishi, K., Sakamoto, M., Ozaki, H., et al., 2020. A 2600-year summer climate reconstruction in central Japan by integrating tree-ring stable oxygen and hydrogen isotopes. *Clim. Past* 16, 2153–2172. <https://doi.org/10.5194/cp-16-2153-2020>.
- Osborn, T.J., Briffa, K.R., Jones, P.D., 1997. Adjusting variance for sample-size in tree-ring chronologies and other regional mean timeseries. *Dendrochronologia* 15, 89–99.
- Pacheco, A., Camarero, J.J., Carrer, M., 2016. Linking wood anatomy and xylogenesis allows pinpointing of climate and drought influences on growth of coexisting conifers in continental Mediterranean climate. *Tree Physiol.* 36, 502–512. <https://doi.org/10.1093/treephys/tpv125>.
- Pandey, S., 2021. Climatic influence on tree wood anatomy: a review. *J. Wood Sci.* 67, 24. <https://doi.org/10.1186/s10086-021-01956-w>.
- Peres-Neto, P.R., Jackson, D.A., Somers, K.M., 2005. How many principal components? Stopping rules for determining the number of non-trivial axes revisited. *Comput. Stat. Data Anal.* 49, 974–997. <https://doi.org/10.1016/j.csda.2004.06.015>.
- Peters, R.L., Balanzategui, D., Hurley, A.G., von Arx, G., Prendin, A.L., Cuny, H.E., Björklund, J., Frank, D.C., Fonti, P., 2018. RAPTOR: Row and position tracheid organizer in R. *Dendrochronologia* 47, 10–16. <https://doi.org/10.1016/j.dendro.2017.10.003>.
- Peters, R.L., Steppe, K., Cuny, H.E., De Pauw, D.J.W., Frank, D.C., Schaub, M., Rathgeber, C.B.K., Cabon, A., Fonti, P., 2021. Turgor – a limiting factor for radial growth in mature conifers along an elevational gradient. *New Phytol.* 229, 213–229. <https://doi.org/10.1111/nph.16872>.
- Prendin, A.L., Petit, G., Carrer, M., Fonti, P., Björklund, J., von Arx, G., 2017. New research perspectives from a novel approach to quantify tracheid wall thickness. *Tree Physiol.* 37, 976–983. <https://doi.org/10.1093/treephys/tpx037>.
- Riechelmann, D.F.C., Greule, M., Treydte, K., Esper, J., Keppler, F., 2016. Climate signals in  $\delta^{13}\text{C}$  of wood lignin methoxyl groups from high-elevation larch trees. *Palaeogeogr. Palaeoclimatol. Palaeoecol.* 445, 60–71. <https://doi.org/10.1016/j.palaeo.2016.01.001>.
- Riechelmann, D.F.C., Greule, M., Siegwolf, R.T.W., Anhäuser, T., Esper, J., Keppler, F., 2017. Warm season precipitation signal in  $\delta^2\text{H}$  values of wood lignin methoxyl groups from high elevation larch trees in Switzerland. *Rapid Commun. Mass Spectrom.* 31, 1589–1598. <https://doi.org/10.1002/rcm.7938>.
- Rinn, F., 2012. *TSAP-win: Time Series Analysis and Presentation for Dendrochronology and Related Applications – Version 4.6x for Microsoft Windows*. Rintech, Heidelberg.
- Robertson, I., Loader, N.J., McCarroll, D., Carter, A.H.C., Cheng, L., Leavitt, S.W., 2004.  $\delta^{13}\text{C}$  of tree-ring lignin as an indirect measure of climate change. *Water Air Soil Pollut. Focus* 4, 531–544. <https://doi.org/10.1023/B:WAF0.0000028376.06179.af>.
- Römer, P., Hartl, C., Schneider, L., Bräuning, A., Szymczak, S., Huneau, F., Lebre, S., Reinig, F., Büntgen, U., Esper, J., 2021. Reduced temperature sensitivity of maximum latewood density formation in high-elevation Corsican pines under recent warming. *Atmosphere* 12, 804. <https://doi.org/10.3390/atmos12070804>.
- Römer, P., Reinig, F., Konter, O., Friedrich, R., Urban, O., Čáslavský, J., Pernicová, N., Trnka, M., Büntgen, U., Esper, J., 2023. Multi-proxy crossdating extends the longest high-elevation tree-ring chronology from the Mediterranean. *Dendrochronologia* 79, 126085. <https://doi.org/10.1016/j.dendro.2023.126085>.
- Spinoni, J., Barbosa, P., De Jager, A., McCormick, N., Naumann, G., Vogt, J.V., 2019. A new global database of meteorological drought events from 1951 to 2016. *J. Hydrol.* 22, 100593. <https://doi.org/10.1016/j.ejrh.2019.100593>.
- Stirbu, M.I., Roibu, C.C., Carrer, M., Mursa, A., Unterholzer, L., Prendin, A.L., 2022. Contrasting climate sensitivity of *Pinus cembra* tree-ring traits in the Carpathians. *Front. Plant Sci.* 13, 855003. <https://doi.org/10.3389/fpls.2022.855003>.
- Szymczak, S., Joachimski, M.M., Bräuning, A., Hetzer, T., Kuhlemann, J., 2012. A 560 yr summer temperature reconstruction for the Western Mediterranean basin based on stable carbon isotopes from *Pinus nigra* ssp. *laricina* (Corsica/France). *Clim. Past* 8, 1737–1749. <https://doi.org/10.5194/cp-8-1737-2012>.
- Torbenson, M.C.A., Büntgen, U., Römer, P., Urban, O., Trnka, M., Ač, A., Reinig, F., Rybníček, M., Kolář, T., Arosio, T., et al., 2023. Assessing earlywood-latewood proportion influence on tree-ring stable isotopes. *Dendrochronologia* 82, 126147. <https://doi.org/10.1016/j.dendro.2023.126147>.
- Treydte, K., Frank, D.C., Esper, J., Andreu, L., Bednarz, Z., Berninger, F., Boettger, T., D'Alessandro, C.M., Etien, N., Filot, M., et al., 2007. Signal strength and climate calibration of a European tree-ring isotope network. *Geophys. Res. Lett.* 34, L24302. <https://doi.org/10.1029/2007GL031106>.
- Vaganov, E.A., 1990. The tracheidogram method in tree-ring analysis and its application. In: Cook, E.R., Kairiukstis, L.A. (Eds.), *Methods of Dendrochronology*. Kluwer, Dordrecht, pp. 63–76.
- von Arx, G., Carrer, M., 2014. Roxas – a new tool to build centuries-long tracheid-lumen chronologies in conifers. *Dendrochronologia* 32, 290–293. <https://doi.org/10.1016/j.dendro.2013.12.001>.
- Wang, Y., Liu, X., Anhäuser, T., Lu, Q., Zeng, X., Zhang, Q., Wang, K., Zhang, L., Zhang, Y., Keppler, F., 2020. Temperature signal recorded in  $\delta^2\text{H}$  and  $\delta^{13}\text{C}$  values of wood lignin methoxyl groups from a permafrost forest in northeastern China. *Sci. Total Environ.* 727, 138558. <https://doi.org/10.1016/j.scitotenv.2020.138558>.
- Wells, N., Goddard, S., Hayes, M.J., 2004. A self-calibrating Palmer drought Severity Index. *J. Clim.* 17, 2335–2351. [https://doi.org/10.1175/1520-0442\(2004\)017<2335:ASPDSI>2.0.CO;2](https://doi.org/10.1175/1520-0442(2004)017<2335:ASPDSI>2.0.CO;2).
- Wieland, A., Greule, M., Römer, P., Esper, J., Keppler, F., 2022. Climate signals in stable carbon and hydrogen isotopes of lignin methoxy groups from southern German beech trees. *Clim. Past* 18, 1849–1866. <https://doi.org/10.5194/cp-18-1849-2022>.
- Wieland, A., Römer, P., Torbenson, M.C.A., Greule, M., Urban, O., Čáslavský, J., Pernicová, N., Trnka, M., Büntgen, U., Esper, J., et al., 2024. Tree-ring stable isotopes in cellulose and lignin methoxy groups reveal different age-related behaviour. *Quat. Int.* 693, 38–48. <https://doi.org/10.1016/j.quaint.2024.02.004>.
- Wigley, T.M.L., Briffa, K.R., Jones, P.D., 1984. On the average of correlated time series, with applications in dendroclimatology and hydrometeorology. *J. Appl. Meteorol. Clim.* 23, 201–213. [https://doi.org/10.1175/1520-0450\(1984\)023<0201:OTAVOC>2.0.CO;2](https://doi.org/10.1175/1520-0450(1984)023<0201:OTAVOC>2.0.CO;2).
- Wilson, A.T., Grinsted, M.J., 1977.  $^{12}\text{C}/^{13}\text{C}$  in cellulose and lignin as palaeothermometers. *Nature* 265, 133–135. <https://doi.org/10.1038/265133a0>.
- Yakir, D., Sternberg, L., 2000. The use of stable isotopes to study ecosystem gas exchange. *Oecologia* 123, 297–311. <https://doi.org/10.1007/s004420051016>.
- Yang, B., Qin, C., Bräuning, A., Osborn, T.J., Trouet, V., Ljungqvist, F.C., Esper, J., Schneider, L., Grießinger, J., Büntgen, U., 2021. Long-term decrease in Asian monsoon rainfall and abrupt climate change events over the past 6,700 years. *Proc. Natl. Acad. Sci. USA* 118, e2102007118. <https://doi.org/10.1073/pnas.2102007118>.
- Young, G.H.F., Demmler, J.C., Gunnarson, B.E., Kirchhefer, A.J., Loader, N.J., McCarroll, D., 2011. Age trends in tree ring growth and isotopic archives: a case study of *Pinus sylvestris* L. from northwestern Norway. *Glob. Biogeochem. Cycles* 25, GB2020. <https://doi.org/10.1029/2010GB003913>.
- Zeisel, S., 1985. Über ein Verfahren zum quantitativen Nachweise von Methoxyl. *Monatsh. Chem.* 6, 989–997. <https://doi.org/10.1007/BF01554683>.
- Zharkov, M.S., Huang, J.G., Yang, B., Babushkina, E.A., Belokopytova, L.V., Vaganov, E.A., Zhirmova, D.F., Ilyin, V.A., Popkova, M.I., Shishov, V.V., 2022. Tracheidogram's classification as a new potential proxy in high-resolution dendroclimatic reconstructions. *Forests* 13, 970. <https://doi.org/10.3390/f13070970>.

- Ziaco, E., 2020. A phenology-based approach to the analysis of conifers intra-annual xylem anatomy in water-limited environments. *Dendrochronologia* 59, 125662. <https://doi.org/10.1016/j.dendro.2019.125662>.
- Ziaco, E., Liang, E., 2019. New perspectives on sub-seasonal xylem anatomical responses to climatic variability. *Trees (Berl.)* 33, 973–975. <https://doi.org/10.1007/s00468-018-1786-9>.
- Ziaco, E., Biondi, F., Rossi, S., Deslauriers, A., 2014. Climatic influences on wood anatomy and tree-ring features of Great Basin conifers at a new mountain observatory. *Appl. Plant Sci.* 2, 1400054. <https://doi.org/10.3732/apps.1400054>.
- Ziaco, E., Biondi, F., Heinrich, I., 2016. Wood cellular dendroclimatology: testing new proxies in Great Basin bristlecone pine. *Front. Plant Sci.* 7, 1602. <https://doi.org/10.3389/fpls.2016.01602>.